Developments in the Built Environment 14 (2023) 100128

Contents lists available at ScienceDirect

Developments in the Built Environment

journal homepage: www.sciencedirect.com/journal/developments-in-the-built-environment

Automated damage diagnosis of concrete jack arch beam using optimized deep stacked autoencoders and multi-sensor fusion

Yang Yu [a,*], Jiantao Li [b], Jianchun Li [c], Yong Xia [d], Zhenghao Ding [d], Bijan Samali [e]

[a] Centre for Infrastructure Engineering and Safety, School of Civil and Environmental Engineering, The University of New South Wales, Sydney, NSW, 2052, Australia
[b] School of Civil Engineering, Zhejiang University of Technology, Hangzhou, Zhejiang, 310000, China
[c] School of Civil and Environmental Engineering, University of Technology Sydney, Ultimo, NSW, 2007, Australia
[d] Department of Civil and Environmental Engineering, The Hong Kong Polytechnic University, Kowloon, Hong Kong, China
[e] Centre for Infrastructure Engineering, Western Sydney University, Penrith, NSW, 2751, Australia

ARTICLE INFO

Keywords:
Structural damage diagnosis
Deep stacked autoencoders
Multi-sensor fusion
Whale optimization algorithm

ABSTRACT

A novel hybrid framework of optimized deep learning models combined with multi-sensor fusion is developed for condition diagnosis of concrete arch beam. The vibration responses of structure are first processed by principal component analysis for dimensionality reduction and noise elimination. Then, the deep network based on stacked autoencoders (SAE) is established at each sensor for initial condition diagnosis, where extracted principal components and corresponding condition categories are inputs and output, respectively. To enhance diagnostic accuracy of proposed deep SAE, an enhanced whale optimization algorithm is proposed to optimize network meta-parameters. Eventually, Dempster-Shafer fusion algorithm is employed to combine initial diagnosis results from each sensor to make a final diagnosis. A miniature structural component of Sydney Harbour Bridge with artificial multiple progressive damages is tested in laboratory. The results demonstrate that the proposed method can detect structural damage accurately, even under the condition of limited sensors and high levels of uncertainties.

1. Introduction

Structural health monitoring (SHM) on civil engineering structures is significant for the safety assessment and maintenance strategies of infrastructure. Vibration-based SHM strategies have been widely studied for identifying and tracing structural damages in the last few decades (Avci et al., 2021; Kamariotis et al., 2023). The applications of vibration response data in SHM can be divided into model-based and data-driven methods. In general, a model-based strategy requires a finite element (FE) model of the structure for a model updating process. Despite its successful and reliable application under certain conditions (Hou et al., 2018; Khayatazad et al., 2020), the mandatory high-fidelity FE model of the structure is difficult or sometimes impossible to be obtained, especially for large-scale and complex structures. Therefore, data driven-based method prevails as a more feasible option (Sen et al., 2019). The time history vibration responses measured from a structure can be analysed in the time, frequency or modal domains as a feature extraction procedure which is often incorporated into a statistical pattern recognition paradigm for damage diagnosis (Entezami and Shariatmadar, 2018). The features should be sensitive to damage and not to environmental and operational variability (EOV), enabling reliable damage detection. In the unmeasurable cases, principal component analysis (PCA)-based methods are commonly employed to reduce or exclude the effects of uncertainty due to EOV (Sohn, 2007; Kullaa, 2011). The PCA also serves as a common feature extraction technique that can be used for dimensionality reduction by data projection (Chen et al., 2020; Ai et al., 2022).

Machine learning (ML) algorithms have been proven as promising data-driven techniques for statistical decision-making in SHM that can broadly be divided into unsupervised and supervised learning types (Caicedo et al., 2022). In the context of SHM, unsupervised methods describe the use of data from only the normal condition of the structure for model training. These methods can be used, for example, to detect the existence of damage (Ma et al., 2020). In contrast, supervised learning methods implement the model learning/training using the data that can be classified and labeled from the undamaged and damaged states (Farrar and Worden, 2012). Supervised methods are capable of detecting the type and/or severity of damages (Flah et al., 2020).

* Corresponding author.
E-mail address: yang.yu12@unsw.edu.au (Y. Yu).

https://doi.org/10.1016/j.dibe.2023.100128
Received 18 October 2022; Received in revised form 18 January 2023; Accepted 31 January 2023
Available online 3 February 2023

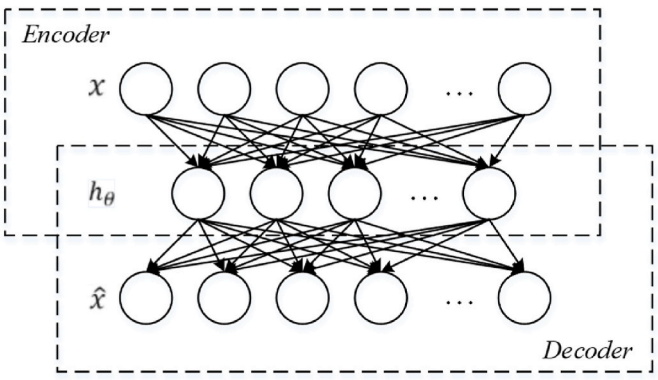

Fig. 1. Schematic diagram of AE.

Furthermore, the extensive implementation of SHM systems on the infrastructure leads to a large number of data in different types and formats, which requires powerful, intelligent and sophisticated computational techniques to analyse the big data (Terzis, 2022).

In recent years, deep learning (DL), a special subfield of ML, has been widely investigated for damage detection and condition assessment of civil infrastructure. Bao et al. proposed a novel structural anomaly detection approach based on computer vision and stacked autoencoders (SAE), the performance of which has been validated using the monitoring data of a real bridge (Bao et al., 2019). Pathirage et al. presented a deep neural network-based framework for damage detection of steel structures, in which sparse autoencoders were used to improve the abilities of feature dimension compression and pattern learning in the pre-training stage (Pathirage et al., 2018, 2019). Liu et al. utilized a similarity-based deep learning method to design an innovative system for defect inspection of railway fasteners. The similarity between pairs of fastener images was adopted to evaluate the extracted features, and the dataset for model training could be enlarged based on the template matching method (Liu et al., 2019). Zhang et al. designed a systematic method to train a recurrent neural network (RNN) for the pixel-level crack identification of pavements (Zhang et al., 2019). Gao et al. adopted a leaf-bootstrapping method to enhance the capacity of a generative adversarial network (GAN) for structural damage check under the condition of confined calculation resource and training dataset (Gao et al., 2019). Yu et al. put forward a highly accurate deep-learning network for segmenting and quantifying concrete surface cracks (Yu et al., 2022a). Li et al. introduced faster region convolutional neural networks (R-CNN) to identify the fine and coarse cracks of the tunnels (Li et al., 2019). Truong et al. proposed a hybridized method consisting of 1-D CNN and gated RNN for vibration-based damage identification of structures in real-time, where 1-D CNN was employed to extract features in spatial scale and gated RNN was utilized to learn the feature in temporal scale and correlate features with target output (Truong et al., 2022a). In addition, an autoencoder-convolutional gated recurrent unit-based deep neural network was designed for damage identification in joints of structures, considering the noise effect (Truong et al., 2022b). Nguyen et al. developed a novel approach based on convolutional long short-term memory (LSTM) neural network to evaluate flexural strength of corroded reinforced concrete (RC) beam (Nguyen et al., 2022). Le et al. put forward a deep neural network for damage diagnosis of composite plates enhanced by functionally graded carbon nanotube, where network inputs are element modal kinetic energy obtained from structural natural frequency and translational nodal displacement (Le et al., 2021). A similar method was also applied to detect multiple damages of functionally graded material-reinforced composite plate (Dinh-Cong et al., 2022). Yu et al. adopted convolutional neural networks (CNN) to develop the predictive model to identify the damage of smart steel structures incorporated with magneto-rheological (MR) devices under seismic loading (Yu et al., 2019). CNN-based approaches were also applied to structural modal analysis (Kim and Sim, 2019; Bao et al., 2020), condition assessment of electricity transmission towers (Dick et al., 2019), dynamic responses prediction of steel frames (Wu and Jahanshahi, 2019), load estimation of offshore platforms (Lyu et al., 2019), residual capacity evaluation (Yu et al., 2022b), SHM data recovery (Fan et al., 2019), and so on.

Although one-fold deep learning methods are capable of achieving satisfactory performance for structural damage identification, they are inclined to perturbation due to various factors such as different datasets, parameter setting of deep learning algorithms, input and output expressions, etc. Among these factors, algorithm parameter setting is the most important, because different parameter combinations may lead to notably different performances of the developed learning models. A group of parameter values may be an optimal choice for a particular case but not for other cases. Accordingly, how to assign the best values of algorithm parameters is a big challenge for the application of DL methods to structural damage detection. On the other hand, the outputs of the trained models are perhaps inaccurate due to sensor fault or data submerged by background noises. In this connection, multiple sensors are generally deployed at various locations to improve diagnosis accuracy. However, the sensors at different locations may generate conflicting results on the structural condition, which increases the challenges for the system to offer accurate evaluation.

Aiming to solve aforementioned issues, this paper puts forward a hybrid approach to structural damage diagnosis using vibration responses. To start with, the PCA-based data whitening procedure is applied to raw vibration signals to avoid the redundancy and correlation of information in signals. Then, the diagnosis model based on deep stacked autoencoder (DSAE) is established at each sensor for providing the evaluation result of the structural condition individually. To enhance the generalization capacity of the proposed diagnosis model, the enhanced whale optimization algorithm (EWOA) is employed to optimize the meta-parameters of DSAE, including dropout parameter, weight decay coefficient, learning rate and neuron numbers of hidden layers. Afterward, the diagnosis results of each sensor are combined to obtain a more accurate structural condition using the Dempster-Shafer (D-S) fusion algorithm. An experimental study is conducted on a scaled model of a real bridge component. The results demonstrate that the proposed hybrid method can realize reliable and accurate diagnosis results and provide a feasible solution to the in-situ evaluation of structural health condition.

2. Preliminaries

2.1. Deep stacked autoencoder

The deep stacked autoencoder is a type of deep neural network composed of multiple layers of autoencoders (AEs) (Lakshmi and Ponnusamy, 2021), the schematic of which is shown in Fig. 1. The AE can be divided into two parts: the encoder and decoder. The neurons in the same layer are independent of each other, while the neurons of adjacent layers are interconnected. The encoder is composed of an input layer, a hidden layer and mapping function between them. The output of hidden layers can be expressed as follows:

$$h_\theta(x) = f(Wx + b) \tag{1}$$

where $f(\cdot)$ denotes the activation function of the encoder, W denotes the encoding weight matrix, x is the input, and b is the bias vector. The decoder is made up of a hidden layer, an output layer and mapping function between them, which is a reverse process of the encoder. The function of the decoder is to transform the output of hidden layer back to the input layer by the mapping function. Accordingly, the output signal can be regarded as the reconstructed signal, denoted by $\hat{x}$. The mapping relationship can be expressed in Eq. (2):

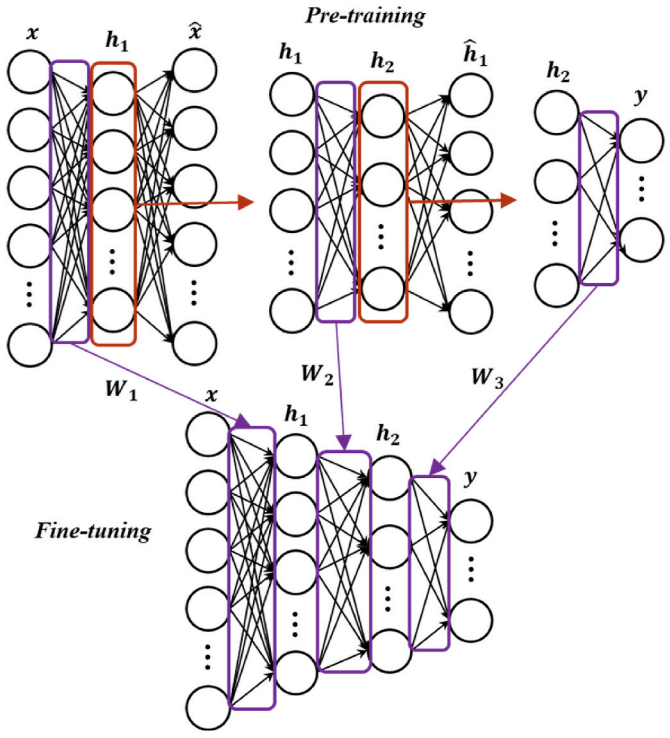

Fig. 2. Schematic diagram of DSAE training.

$$\hat{x}_{\theta'}(h) = g(W^* h + b^*) \tag{2}$$

where $g(\cdot)$ denotes the activation function of the decoder, W^* is the decoding weight matrix, and b^* is the decoding bias vector. In order to evaluate the reconstruction effect of AE, the mean square error (MSE) is adopted to define the loss function with the following expression:

$$C_0(W, b; x, \hat{x}) = \frac{1}{2}\|x - \hat{x}\|^2 \tag{3}$$

Given a data set with N samples, the loss function can be defined as:

$$C(W, b) = \frac{1}{N}\sum_{k=1}^{N} C_0(W, b, x_k, \hat{x}_k)\Bigg) \tag{4}$$

where x_k denotes the kth input.

For the complicated problem of high dimensionality, it is hard to extract nonlinear characteristics of inputs based on the network of AE. To gain high-level abstraction of input data, a network with deep architecture consisting of multiple AEs is needed, which is also called deep stacked autoencoder (DSAE). The training of DSAE is mainly composed of two stages: unsupervised layer-by-layer pre-training and supervised reverse fine-tuning, as shown in Fig. 2. Both strategies are able to improve the learning accuracy and learning rate of the model. However, given certain training samples, to learn more effective features, the training time of the DSAE always increases, which is prone to over-training. Over-training can cause the over-fitting phenomenon of high classification accuracy of training samples and low classification accuracy of testing samples. To solve this problem, two operations are introduced to the DSAE during the training procedure.

The first operation is dropout, which takes the mean value of multiple model predictions so that the weight updating is no longer dependent on the combined action of neurons with fixed relationship. The neurons in the hidden layers are randomly discarded with the probability p_d to form a sub-network of the initial network. The discarded matrix $D = \{D_1, D_2, \ldots, D_n\}$ complies with the Bernoulli distribution and its probability distribution function is:

$$P(k; p_d) = \begin{cases} p_d, k = 1 \\ 1 - p_d, k = 0 \end{cases} \tag{5}$$

where k denotes the possible output. Then, the dropout method is introduced into each hidden layer, and the mapping function of the initial neural network coding process can be changed by the following expression:

$$h_i(x) = D_i f\left(\sum_{k=1}^{n} WX_i + b\right) = \begin{cases} f\left(\sum_{k=1}^{n} WX_i + b\right), D_i = 1 \\ 0, \quad D_i = 0 \end{cases} \tag{6}$$

The second operation for solving the over-fitting problem is to add a weight decay coefficient in the loss function (Eq. (4)), which is also called l_2 regularization item. Then, the modified overall loss function can be expressed by:

$$C(W, b) = CCE + \frac{\lambda}{2}\sum_{p=1}^{L-1}\sum_{j=1}^{s_p}\sum_{i=1}^{s_{p+1}}\left(W_{ij}^{(p)}\right)^2 \tag{7}$$

where the first item is the categorical cross-entropy function, which is conventional loss function for multi-label classification, as shown in Eq. (8), and the second is to evaluate the weight decay by summing up the squares of all weights. $W_{ij}^{(p)}$ denotes the connection weight between the jth neuron in the pth layer and the ith neuron in the $(p+1)$th layer, λ denotes the weight decay coefficient, and s_p is the total number of neurons in the pth layer.

$$CCE = -\frac{1}{N}\sum_{k=1}^{N}\sum_{m=1}^{N_{cc}} y_{ij} \bullet \log\left(\hat{y}_{ij}\right) \tag{8}$$

where y and $\hat{y}$ denote real and predicted labels, N_{cc} and denotes the label number. In the DSAE model, critical parameters (or meta-parameters), such as numbers of hidden neurons, weight decay coefficient, dropout parameter and learning rate, significantly affect the model performance. Minimization of the reconstruction error of AEs is generally used as an effective method to find the optimal parameters.

2.2. Enhanced whale optimization algorithm

The WOA is a novel heuristic optimization algorithm proposed by Mirjalili and Lewis, which is based on the mathematical simulation of hunting behaviour of humpback whales (Mirjalili and Lewis, 2016). In the WOA, the location of each humpback whale represents a feasible solution. The mathematical model of the WOA mainly includes three behaviours: encircling prey, bubble-net exploitation, and prey exploration. The behaviour of encircling prey is formulated as follows:

$$\begin{aligned} Y(t+1) &= Y^*(t) - A \bullet |2r \bullet Y^*(t) - Y(t)| \\ A &= 2a \bullet r - a \end{aligned} \tag{9}$$

where $Y(t)$ denotes the location vector of the whale at the current iteration number t, $Y^*(t)$ is the optimal value of $Y(t)$, a is a variable with the value decreasing from 2 to 0, and r denotes a random number between 0 and 1. The behaviour of bubble-net exploitation can be expressed by:

$$Y(t+1) = \begin{cases} Y^*(t) - A \bullet |2r \bullet Y^*(t) - Y(t)|, p < 0.5 \\ Y^*(t) + |Y^*(t) - Y(t)| \bullet e^{bl} \bullet \cos(2\pi l), p \geq 0.5 \end{cases} \tag{10}$$

where b is a constant to define the spiral shape, l and p are two random numbers between 0 and 1. The expression of prey exploration is shown as:

$$Y(t+1) = Y_{rand} - A \bullet |2r \bullet Y_{rand} - Y(t)| \tag{11}$$

where Y_{rand} denotes the location of a randomly selected whale. The whale will follow behaviour of bubble-net exploitation if $|A| < 1$, or prey

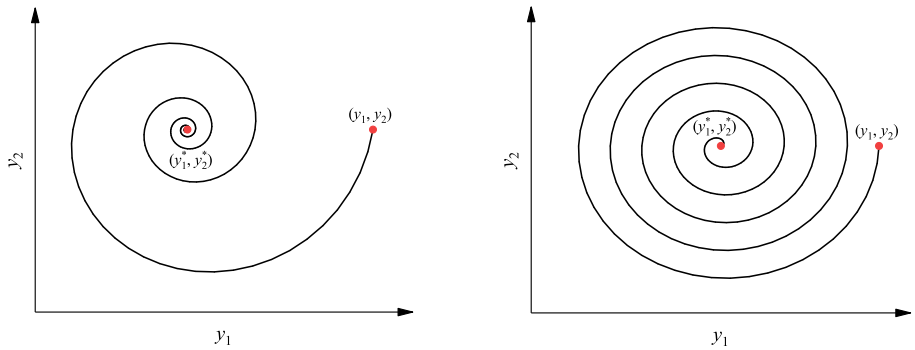

(a) Logarithmic spiral curve (b) Archimedean spiral curve

Fig. 3. 2-D examples of two types of spiral curves

Based on the above improvements, the procedure of the proposed EWOA can be summarized as the following steps.

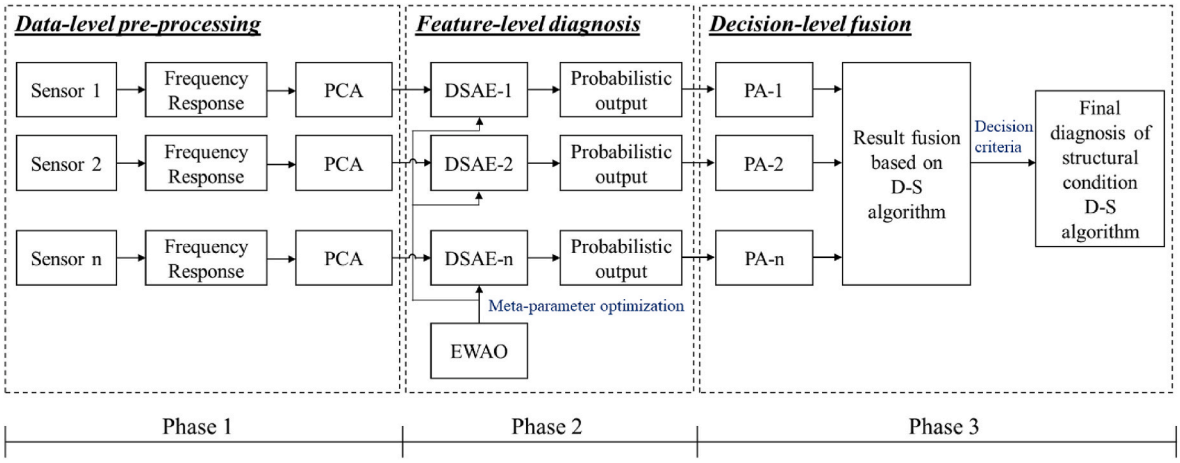

Fig. 4. Schematic diagram of proposed hybrid framework for structural damage diagnosis.

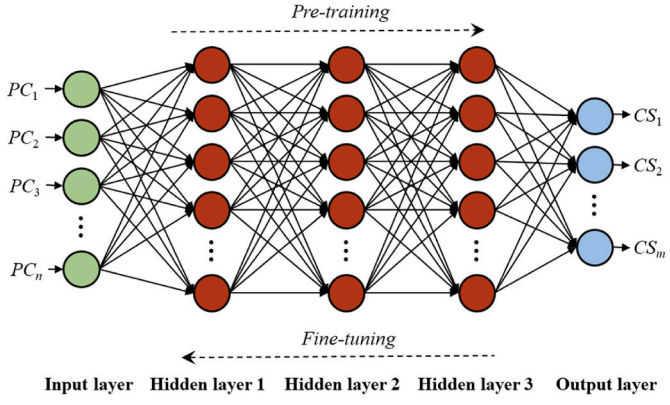

Fig. 5. Architecture of proposed DASE model for structural damage diagnosis at each sensor.

exploration otherwise.

Even though the WOA has been widely applied in solving various engineering problems due to the benefit of easy implementation, it has the problems of slow convergence rate and low calculation accuracy when dealing with complex optimization problems. There are two possible factors resulting in this phenomenon. The first factor is the random research strategy in the WOA, which can cause slow convergence in spite of the good global search ability. The second reason is the logarithmic spiral curve used for location update in Eq. (10), which makes the humpback whale unable to sufficiently explore all the space within its range. To resolve these problems, an enhanced WOA (EWOA) is proposed in this study, in which a self-adaptive inertia weight and equal pitch Archimedean spiral curve are added to the original WOA to improve the algorithm accuracy. The self-adaptive inertia weight can enhance the local search ability of algorithm, with the following expression:

$$iw = iw_{max} - (iw_{max} - iw_{min})\left(\frac{t}{T_{max}}\right)^{\frac{1}{i}} \tag{12}$$

where iw_{max} and iw_{min} denote maximum and minimum inertia weights, respectively, and T_{max} denotes the maximum iteration number. In this regard, Eq. (9) can be reformulated as

$$Y(t+1) = \begin{cases} iw \bullet Y^*(t) - A \bullet |2r \bullet Y^*(t) - Y(t)|, p < 0.5 \\ iw \bullet Y^*(t) + |Y^*(t) - Y(t)| \bullet e^{bl} \bullet \cos(2\pi l), p \geq 0.5 \end{cases} \tag{13}$$

It is noticeable from Eq. (11) that the inertia weight nonlinearly decreases with the increase of the iteration number. In the initial iteration stage, the inertia weight is large, so the algorithm has a good global search ability, which makes the whale quickly approach the approximate area of the prey (best solution). In the later iteration stage, the inertia weight gradually decreases, which indicates a good local search ability. This can effectively improve the accuracy of the optimization result.

In addition, in the WOA the humpback whale swims towards the prey in a logarithmic spiral curve path. Fig. 3 (a) demonstrates this principle for a 2-D case, where the location (y_1, y_2) of a humpback whale is updated in accordance with the current optimal location (y_1^*, y_2^*) using

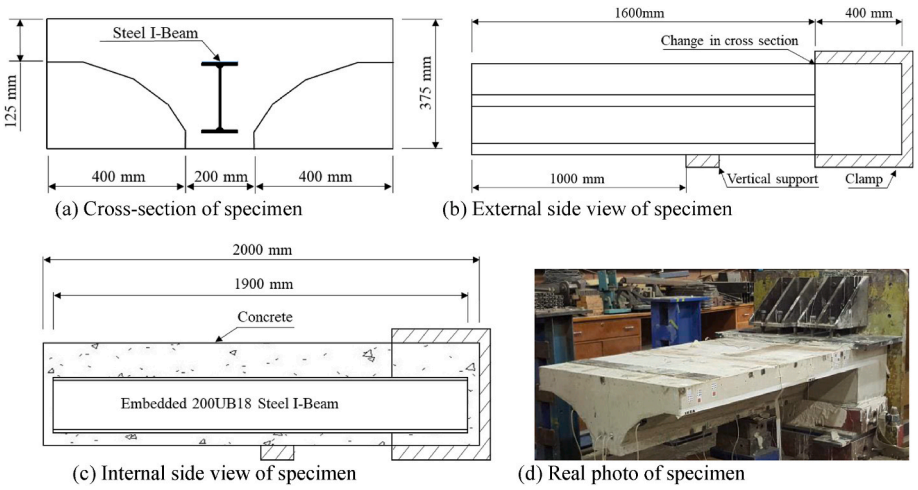

Fig. 6. Design and photo of cantilever beam with an arch section.

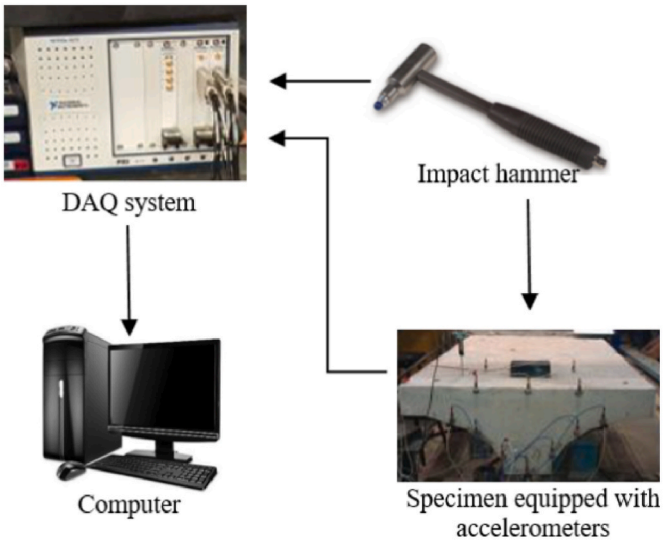

Fig. 7. Experimental setup.

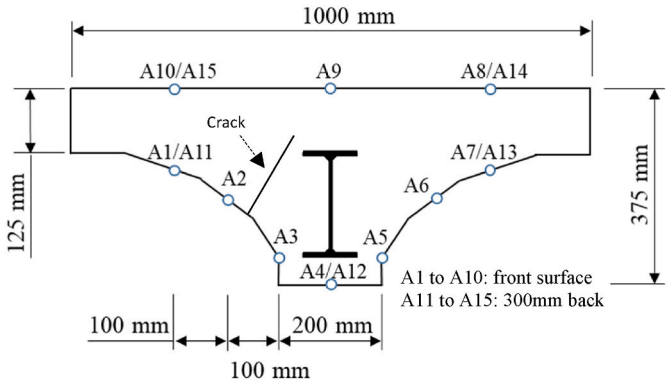

Fig. 8. Schematic diagram of sensor deployment.

Eq. (10). However, the logarithmic spiral curve path is asymmetric in the 2-D space. Any location near the optimal whale could be varied by changing the values of coefficient variables a and r. If the spiral curve's pitch is smaller than that of the humpback whale, some areas could not be searched due to poor algorithm periodicity. Aiming at addressing this

Table 1
Detailed conditions of the specimen.

Index	Condition	Description
CS1	Intact	No crack
CS2	Small damage	The crack is 75 mm long
CS3	Moderate damage	The crack is 150 mm long
CS4	Large damage	The crack is 225 mm long
CS5	Severe damage	The crack is 270 mm long

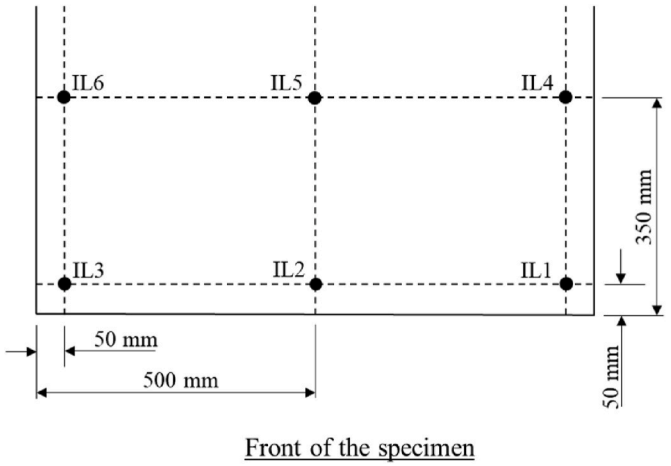

Fig. 9. Hammer impact locations.

issue, this study employs the Archimedean spiral curve to replace the logarithmic spiral curve in the WOA, which is shown as follows.

$$\begin{cases} y_1 = (a_0 + b \bullet l)\cos(2\pi l) \\ y_2 = (a_0 + b \bullet l)\sin(2\pi l) \end{cases} \tag{14}$$

Fig. 3 (b) displays an example of Archimedean spiral curve when $a_0 = 0$ and $b = 1$. As can be seen from the figure, the pitch of the spiral curve is a constant, which can be easily adjusted to obtain optimal performance.

With the introduction of Eq. (13), Eq. (12) can be rewritten as

$$Y(t+1) = \begin{cases} iw \bullet Y^*(t) - A \bullet |2r \bullet Y^*(t) - Y(t)|, p < 0.5 \\ iw \bullet Y^*(t) + |Y^*(t) - Y(t)| \bullet (a_0 + b \bullet l) \bullet \cos(2\pi l), p \geq 0.5 \end{cases} \tag{15}$$

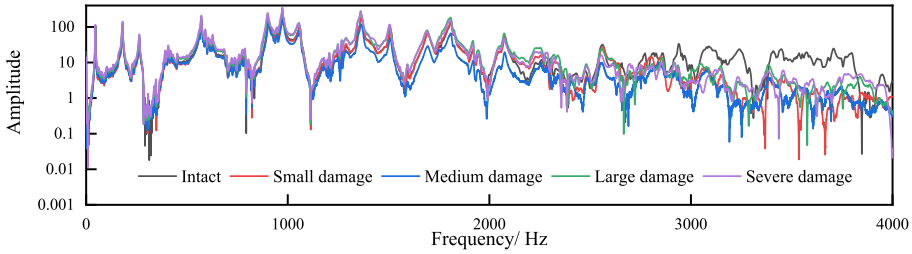

Fig. 10. Comparison of FFT responses corresponding to different condition scenarios.

Table 2
The first six frequencies of the specimen in intact and damaged conditions.

Mode No.	Structural condition scenarios								
	CS1	CS2		CS3		CS4		CS5	
	NF (Hz)	*NF* (Hz)	*ROC* (%)	*NF* (Hz)	*ROC* (%)	*NF* (Hz)	*ROC* (%)	*NF* (Hz)	*ROC* (%)
1	44.81	45.15	0.089	45.12	0.155	45.16	0.288	44.59	0.664
2	179.77	179.81	0.033	179.51	0.145	178.97	0.445	178.78	0.551
3	270.22	270.86	0.133	271.72	0.184	270.13	0.354	270.26	0.402
4	571.21	570.97	0.042	570.27	0.165	570.16	0.184	570.04	0.205
5	904.12	903.27	0.094	900.89	0.357	899.44	0.518	896.22	0.874
6	973.61	973.58	0.003	973.17	0.045	971.77	0.189	970.76	0.293
Averaged *ROC* (%)		0.065		0.175		0.329		0.498	

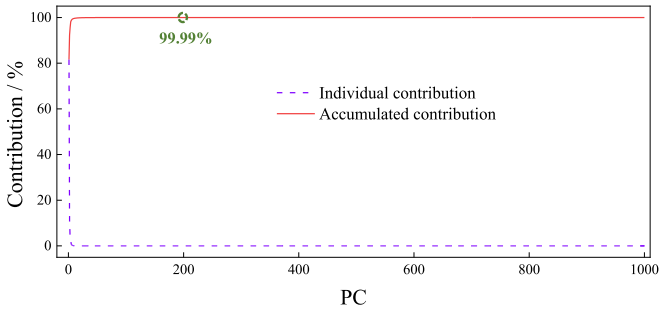

Fig. 11. Individual and accumulated contributions of PCs of FFT responses of signals from Sensor A1.

Step 1. Set the size of the whale swarm N_p and maximum iteration number N_{max}. Initialize the algorithm parameters: a, r, l, a_0, b and p.
Step 2. The fitness values of N_p whales are calculated and compared to obtain the optimal individual with best fitness, represented by Y^*.
Step 3. Enter the main loop of the algorithm. If $|A| < 1$, the location of the whale is updated according to Eq. (15). Otherwise, the location of the whale is updated according to Eq. (11).
Step 4. Re-evaluate the fitness values of all whales in the swarm to find the globally optimal individual with corresponding location. If the current optimal fitness is better than the previous one, replace the previous optimal location with the current one. Otherwise, keep the optimal individual and location unchanged.
Step 5. Check the algorithm-stopping criterion. In this study, the maximum iteration is employed as the termination criterion. If the current iteration number is larger than the maximum number, the algorithm will terminate; or else, go to Step 2 and continue the algorithm iteration.
Step 6. Output the optimal solution Y^*.

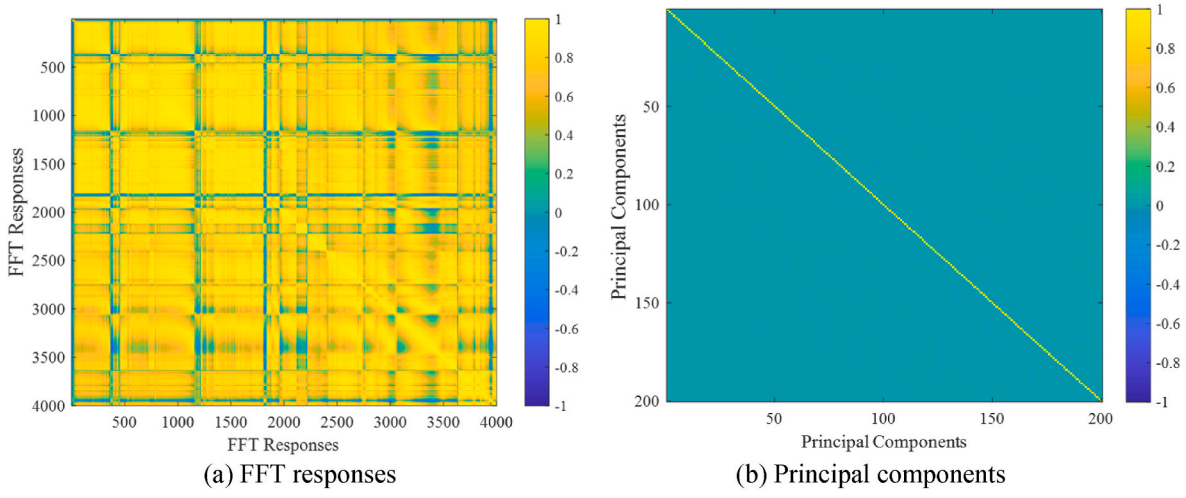

Fig. 12. Heatmap of correlation coefficient matrix of model inputs.

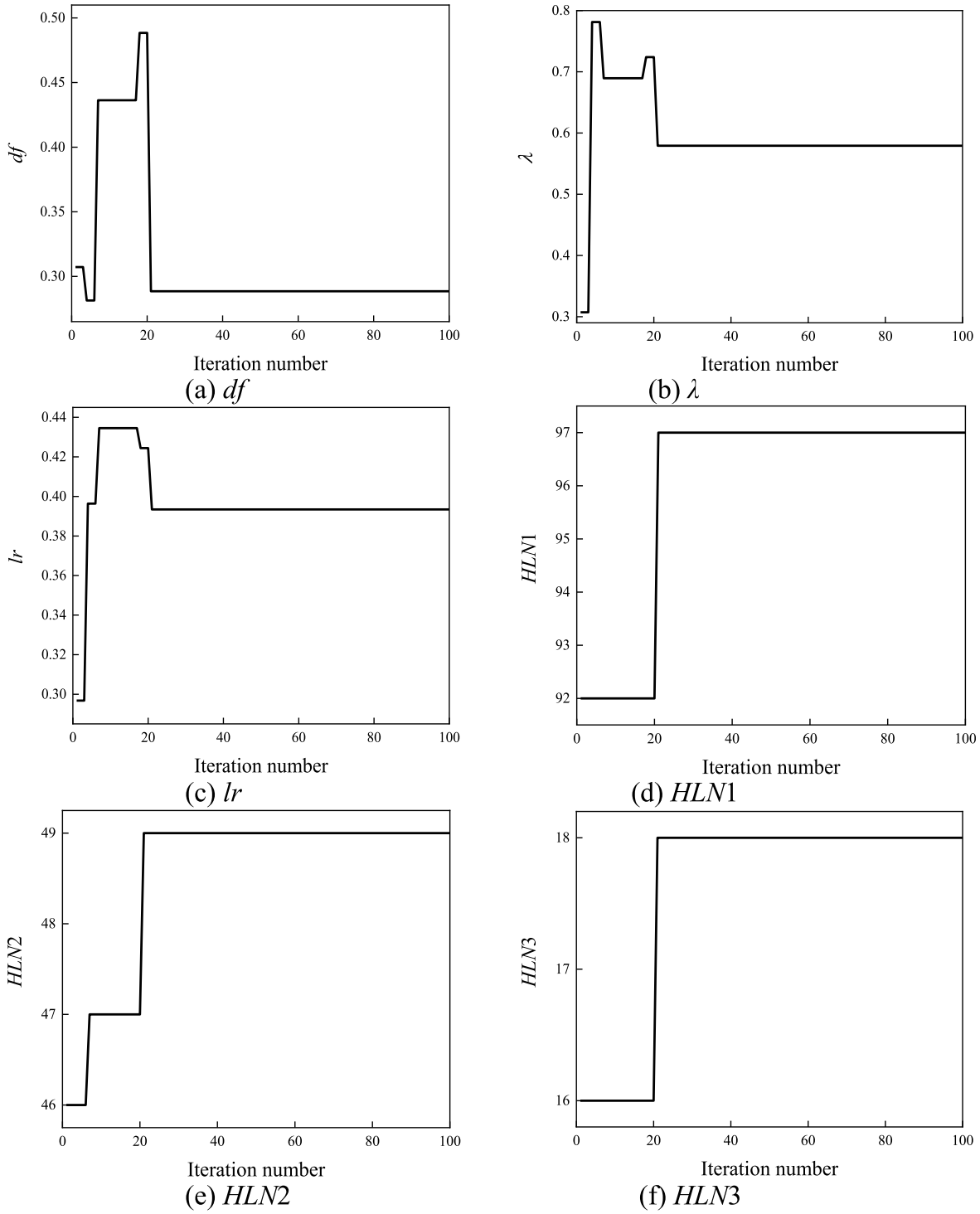

Fig. 13. Meta-parameter optimization of EWOA−DSAE−1.

The performance of the proposed EWOA has been validated based on benchmark test functions via a comparison with other homogeneous algorithms, and relevant results and discussions can be found in Appendix.

2.3. D-S fusion method

The D-S fusion method, proposed by Dempster and Shafer, is a type of uncertain reasoning approach and allows the whole problem and evidence to be divided into several sub-problems and sub evidences (Dempster, 2008; Shafer, 1976). After dealing with the sub-problems and sub evidences, the solution to the whole problem can be obtained by using the D-S combination rule. The fundamental of D-S fusion can be summarized as follows. Given a frame of discernment Θ, the set function m is a mapping on the power set 2^{Θ} of the frame of discernment $m: 2^{\Theta} \rightarrow [0,1]$. If $m(\varnothing) = 0$ and $\sum_{X \subseteq \Theta} m(X) = 1$, m is called basic probability assignment (PA) of Θ, which reflects the reliability degree of X. Suppose $m_1, m_2, \ldots, m_n$ denote the corresponding basic PAs of the frame of discernment Θ, and $X_1, X_2, \ldots, X_n$ denote the corresponding focal elements. The PA $m(X)$ after evidence combination can be expressed as

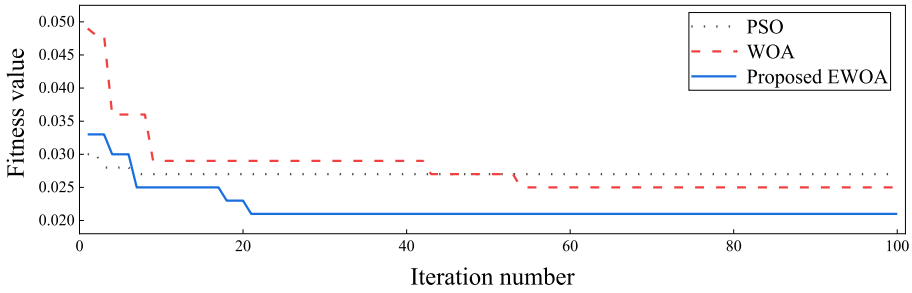

Fig. 14. Convergence of different algorithms for optimizing meta-parameters of EWOA−DSAE−1.

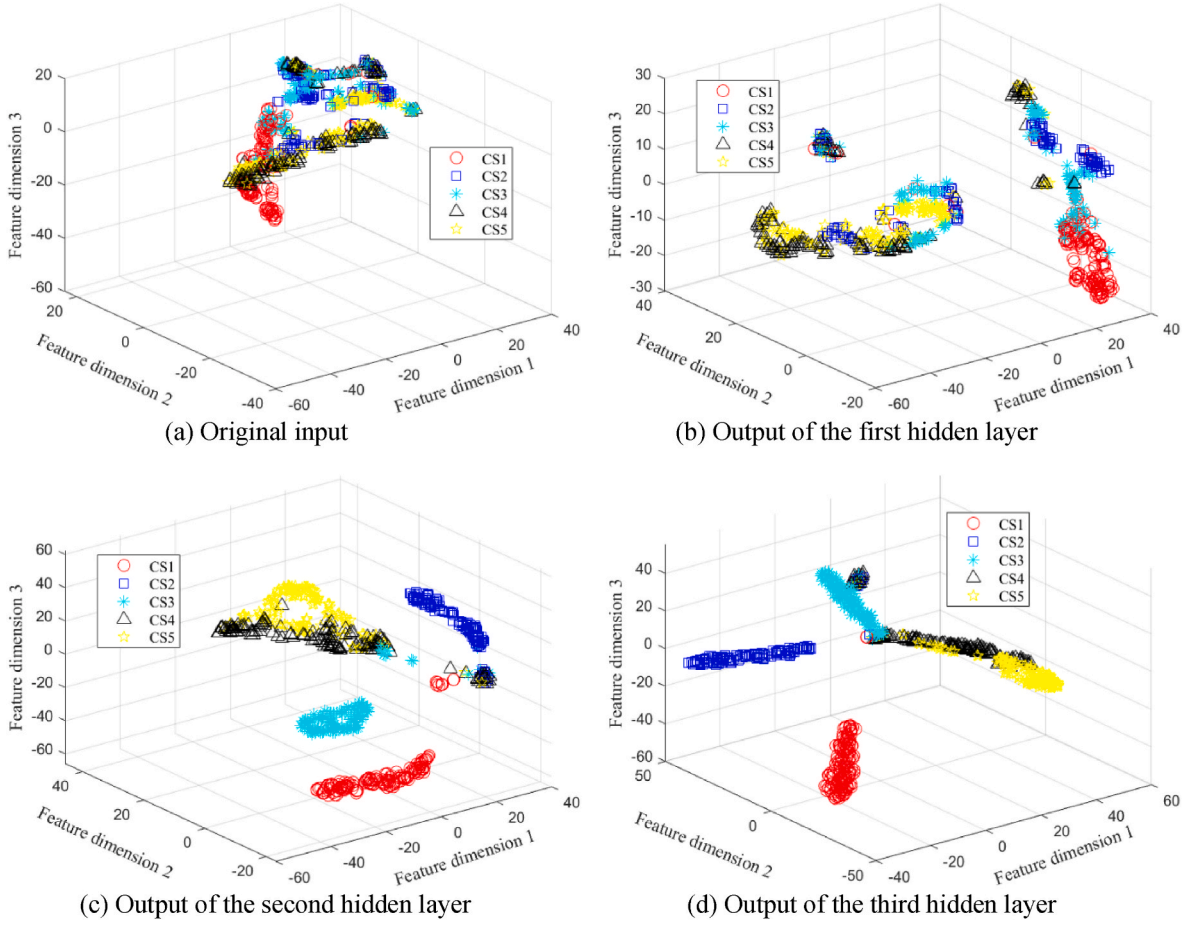

Fig. 15. Feature visualization of EWOA−DSAE−1.

Table 3
Evaluation results of four learning models.

Model	Evaluation index		
	Accuracy	Macro-F_1	Micro-F_1
DSAE	0.9648	0.9143	0.9120
CNN	0.9744	0.9373	0.9360
SVM	0.9584	0.9069	0.8960
Proposed	0.9776	0.9455	0.9440

follows.

$$m(X) = \begin{cases} \dfrac{\sum_{A=X} m_1(X_1)m_2(X_2)\cdots m_n(X_n)}{1-\sum_{A=\varnothing} m_1(X_1)m_2(X_2)\cdots m_n(X_n)}, X \neq \varnothing \\ 0, X = \varnothing \end{cases} \tag{16}$$

$$A = X_1 \bigcap X_2 \bigcap \cdots \bigcap X_n$$

where $k = 1 - \sum_{A=\varnothing} m_1(X_1)m_2(X_2)\cdots m_n(X_n)$ denotes the conflict factor, and the value is between 0 and 1.

The maximal PA is used to set the criteria for decision-making, which meets the following rules:

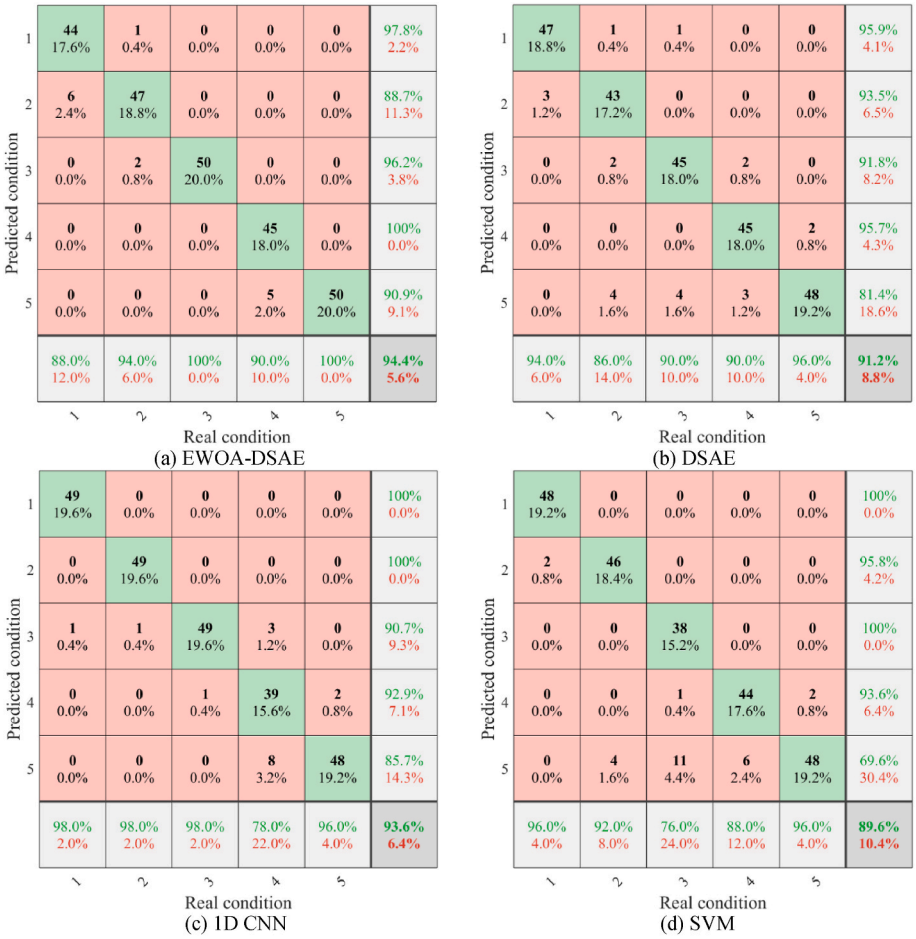

Fig. 16. Comparison of confusion matrices of different learning models.

1) The target scheme has the maximum PA, i.e., $m(X_1) = \max\{m(X_i), X_i \subset \Theta\}$.
2) The difference of PAs between the target scheme and other schemes should be large enough, i.e., $m(X_1) - m(X_2) > \varepsilon_1$, where $m(X_2) = \max\{m(X_i), X_i \subset \Theta, X_i \neq X_1\}$.
3) The PA of uncertainty should be less than a certain threshold, i.e., $m(\Theta) < \varepsilon_2$.

3. Methodology

In this study, a hybrid framework based on SAE-based deep neural networks and D-S data fusion algorithm is developed to process the vibration responses for structural damage diagnosis. The proposed framework consists of three phases: data-level pre-processing, feature-level diagnosis and decision-level fusion. The schematic framework is shown in Fig. 4.

In the data-level phase, the vibration signals in the frequency domain are selected for pre-processing due to the sparse characteristics. A whitening operation is applied to the frequency domain data to eliminate the redundant and correlated information so that the processed data have a uniform identity variance. Here, PCA is employed to implement this task, where original frequency-domain signals are represented by limited number of predominant components (Wold et al., 1987, Şimşek et al., 2021). The obtained PCs are orthogonal to each other and sorted in descending order of contribution. The transformation formula of the PCA is given as follows:

$$z_{pca,i}(k) = \frac{H^T z(k)}{\sqrt{\xi_i}} \tag{17}$$

where $z(k)$ is the kth sample with the dimension of i; H is the transformation matrix; and ξ_i denotes the ith eigenvalue of the covariance of z. By discarding PCs with least contributions, the redundant information in the original data set is eliminated.

In the feature-level phase, the extracted PCs, as the data characteristics, together with the corresponding categories of structural condition, are used to build up the DSAE model for each sensor. The main reason for employing the decentralised/distributed data processing strategy is that compared to conventional centralised processing method, decentralised/distributed strategy is able to effectively reduce data transmission and doesn't need high requirement of processing unit and memory of sensing system, which can be easily implemented in existing structural health monitoring network system based on Internet of Things (IoT). The architecture of deep neural networks based on SAE is shown in Fig. 5. It is clearly seen that the proposed DSAE is composed of five layers, including one input layer, three hidden layers and one output layer. The inputs of DSAE are PCs extracted in the first phase, while the output is a probability vector of potential condition scenarios (CS) of the structure. As mentioned in Section 2.1, the meta-parameters in the DSAE have significant influences on the feature extraction and generalization ability of trained models. Improper assignments of meta-parameters may result in the degradation of model performance. Additionally, meta-parameters, performing well for a particular data set, may not produce a similar performance for different sets of data collected from different sensors. Accordingly, it is of great significance to select optimal meta-parameters for different data applications. The meta-parameters of DSAE to be optimized include the neuron numbers of different hidden layers, weight decay coefficient, dropout parameter and learning rate. In this study, the EWOA is employed to implement the

Table 4
Identification results of the EWOA−DSAE models corresponding to different accelerometers.

Model ID	Identification accuracy		
	Training data	Validation data	Total
EWOA−DSAE−1	92.40% (693/750)	94.40% (236/250)	92.90% (929/1000)
EWOA−DSAE−2	83.87% (629/750)	84.80% (212/250)	84.10% (841/1000)
EWOA−DSAE−3	92.53% (694/750)	95.60% (239/250)	93.30% (933/1000)
EWOA−DSAE−4	79.97% (593/750)	78% (195/250)	78.80% (788/1000)
EWOA−DSAE−5	92.13% (691/750)	94.40% (236/250)	92.70% (927/1000)
EWOA−DSAE−6	89.60% (672/750)	87.20% (218/250)	89% (890/1000)
EWOA−DSAE−7	96.27% (722/750)	98.40% (246/250)	96.80% (968/1000)
EWOA−DSAE−8	90.40% (678/750)	87.60% (219/250)	89.70% (897/1000)
EWOA−DSAE−9	90.67% (680/750)	88.80% (222/250)	90.20% (902/1000)
EWOA−DSAE−10	81.33% (610/750)	76.80% (192/250)	80.20% (802/1000)
EWOA−DSAE−11	84.40% (633/750)	84% (210/250)	84.30% (843/1000)
EWOA−DSAE−12	92.13% (691/750)	95.20% (238/250)	92.90% (929/1000)
EWOA−DSAE−13	92.27% (692/750)	94.80% (237/250)	92.90% (929/1000)
EWOA−DSAE−14	93.33% (700/750)	97.60% (244/250)	94.40% (944/1000)
EWOA−DSAE−15	92.40% (693/750)	94.80% (237/250)	93% (930/1000)

Table 5
PAs of a validation case under small damage condition.

PA	CS1	CS2	CS3	CS4	CS5	Θ
m_1	0.0352	0.9619	0.0025	0.0003	0.0000	0.0000
m_2	**0.7539**	**0.2245**	**0.0183**	**0.0007**	**0.0025**	**0.0000**
m_3	0.0045	0.9950	0.0000	0.0005	0.0000	0.0000
m_4	**0.4873**	**0.5002**	**0.0069**	**0.0032**	**0.0025**	**0.0000**
m_5	0.0035	0.8007	0.1681	0.0275	0.0003	0.0000
m_6	0.0892	0.8763	0.0034	0.0309	0.0003	0.0000
m_7	0.0000	0.9971	0.0007	0.0021	0.0001	0.0000
m_8	**0.6787**	**0.3173**	**0.0032**	**0.0008**	**0.0000**	**0.0000**
m_9	0.0001	0.9847	0.0147	0.0002	0.0002	0.0000
m_{10}	0.2029	0.7946	0.0005	0.0019	0.0001	0.0000
m_{11}	0.2856	0.4837	0.0496	0.1500	0.0312	0.0000
m_{12}	0.0715	0.9105	0.0165	0.0012	0.0003	0.0000
m_{13}	**0.5372**	**0.3552**	**0.0093**	**0.0631**	**0.0353**	**0.0000**
m_{14}	0.0769	0.9185	0.0044	0.0002	0.0000	0.0000
m_{15}	0.0189	0.8398	0.1192	0.0206	0.0014	0.0000

*Note: bold numbers denote the abnormal results.

Table 6
Fusion result of a validation case under small damage condition.

PA	CS1	CS2	CS3	CS4	CS5	Θ
m	0.0000	1.0000	0.0000	0.0000	0.0000	0.0000

optimization of parameters during the training procedure, which is deemed to solve a global optimization problem. The key point is to choose a reasonable objective function for optimal solution. Here, the objective function is designed based on the loss function of DSAE, which is shown in Eq. (18):

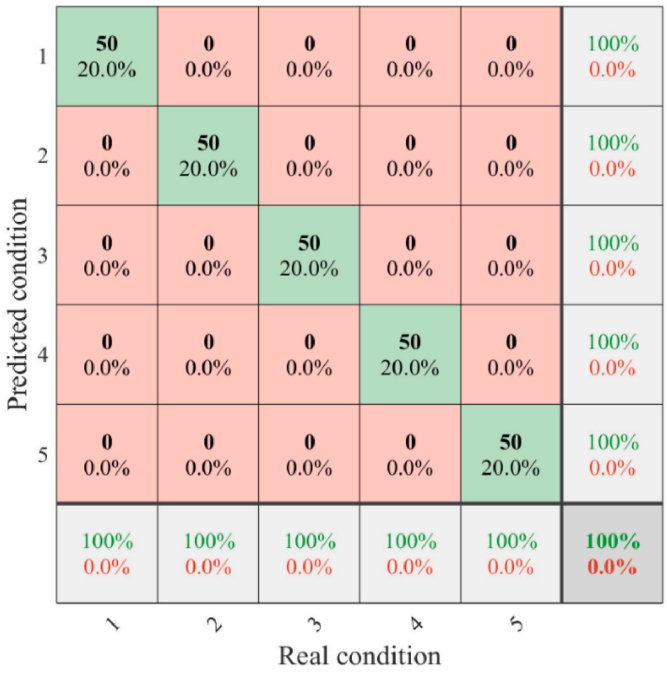

Fig. 17. Confusion matrix of proposed hybrid framework based on validation data.

$$J = 1 - \frac{\sum_{k=1}^{N_{tr}} I\{po(\tilde{y}^k = y^k \lfloor x^k, \delta) > 0.5\}}{N_{tr}} \tag{18}$$

where $\tilde{y}^k$ and y^k denote the predicted and real conditions of kth sample, respectively; $I\{\bullet\}$ is the indicator function, which is 1 for a true input and 0 otherwise; and $po(\tilde{y}^k = y^k \lfloor x^k, \delta)$ denotes the probability of the predicted result belonging to real label by softmax classification, and its expression is given as follows:

$$po(\tilde{y}^k = y^k \lfloor x^k, \delta) = \frac{e^{\delta_i^T x^k}}{\sum_{j=1}^{N_{cc}} e^{\delta_j^T x^k}} \quad (i = 1, 2, \ldots, N_{cc}) \tag{19}$$

where δ_i^T denotes the vector of connection weights and bias of the ith neuron in the output layer, corresponding to the ith structural condition scenario; and N_{cc} denotes the total number of condition scenarios.

To accomplish accurate and comprehensive evaluation of structural condition, the vibration signals from multiple sensors at different locations should be collected and analysed. However, affected by sensor self-fault or environmental uncertainties, the diagnosis results from different sensors may be different, sometimes even conflicting. In this regard, in the decision-level phase the D-S fusion algorithm is used to combine the results from different sensors to deliver a final decision. The probability outputs of all condition scenarios from the DSAE model of each sensor can be considered as individual evidence to construct the PA. The evidence combination of multiple sensors deployed at different locations can effectively improve the diagnosis accuracy of structural condition.

4. Experimental tests and data description

A cantilever beam made of concrete with an arch section was designed and fabricated in Structures Lab, Univerity of Technology Sydney. It is a miniature component of Sydney Harbour Bridge. This specimen was poured by concrete with compressive strength of 32 MPa. A 200UB18 steel I-Beam was embedded inside the specimen with 50 mm concrete cover on both ends. The structure is 2.0 m long in total, with a

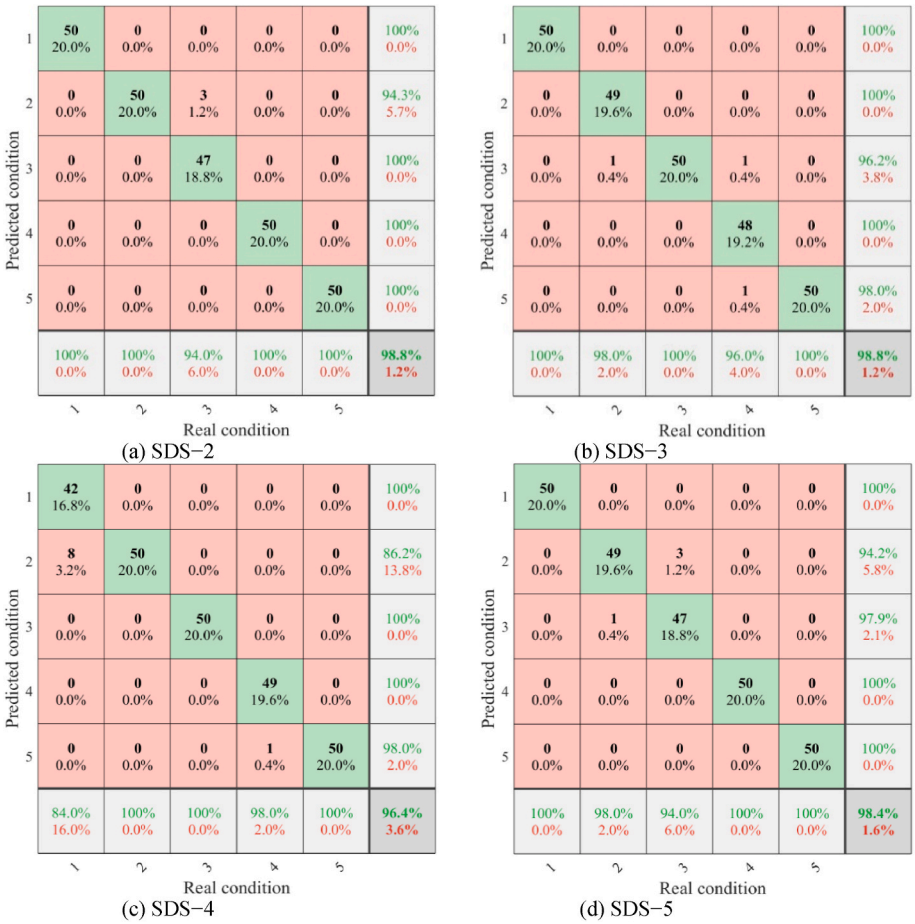

Fig. 18. Confusion matrix of different sensor deployment scenarios.

Table 7
Values of evaluation indices of different deployment scenarios.

Deployment scenario	Evaluation index		
	Accuracy	Macro-F_1	Micro-F_1
SDS−1	1.0000	1.0000	1.0000
SDS−2	0.9952	0.9883	0.9880
SDS−3	0.9952	0.9882	0.9880
SDS−4	0.9856	0.9662	0.9640
SDS−5	0.9936	0.9841	0.9840

Table 8
PAs of a large damage case under the scenario SDS−2 with uncertainty level of 50%.

PA	CS1	CS2	CS3	CS4	CS5	Θ
m_2^*	0.0000	0.0001	0.0001	0.1838	0.3159	0.5000
m_3^*	0.0000	0.0013	0.0000	0.4979	0.0008	0.5000
m_9^*	0.0000	0.0001	0.0086	0.4901	0.0011	0.5000

Table 9
Fusion result of a large damage case under the scenario SDS−2 with uncertainty level of 50%.

PA	CS1	CS2	CS3	CS4	CS5	Θ
m^*	0.0000	0.0005	0.0029	0.7265	0.1052	0.1649

1.6 m long arch cross-section and a 0.4 m long rectangular block fixed to a large steel clamp. The detailed design of the specimen can be found in Fig. 6.

This arch cantilever specimen with introduced artificial damage is used to validate the proposed diagnostic framework. The experimental setup is shown in Fig. 7. An impact hammer of model PCB086D05 was utilized to excite the specimen at several reference locations, and fifteen PCB 352C34 piezoelectric accelerometers were deployed at different locations of the specimen (denoted as A1 to A15 in Fig. 8) to capture the structural vibration responses. For accelerometers A1 to A10, they were placed at the tip of arch cantilever beam; for accelerometers A11 to A15, they were deployed 300 mm from the tip of beam. The signals of the hammer and accelerometers were subsequently sent to the data acquisition (DAQ) system. The DAQ system is comprised of a PXIe-1073 chassis, including two PXIe-4492 vibration and sound modules, which contain a signal conditioner and built-in antialiasing filters. With each hammer strike, the DAQ system sent discrete time-domain signals to the computer system. For each test, the sampling rate was set to 8 kHz with 16,000 time-domain data points being recorded, leading to a frequency range of 0–4 kHz with 8000 data points.

After the specimen was tested in intact condition, artificial damages were incrementally introduced to the structure by an electric motor saw to produce multiple damage scenarios. The damage location is between accelerometers A2 and A3 with a cut depth of 55 mm (crack width), as shown in Fig. 8. In this study, five condition scenarios are considered, including intact condition and four damage conditions with different crack lengths, as detailed in Table 1. There are six hammer excitation reference points, shown in Fig. 9 denoted by IL1 to IL6. At impact location 1 (IL1), 150 hammer strikes were conducted on the specimen for each condition scenario, and the collected data (impact force and

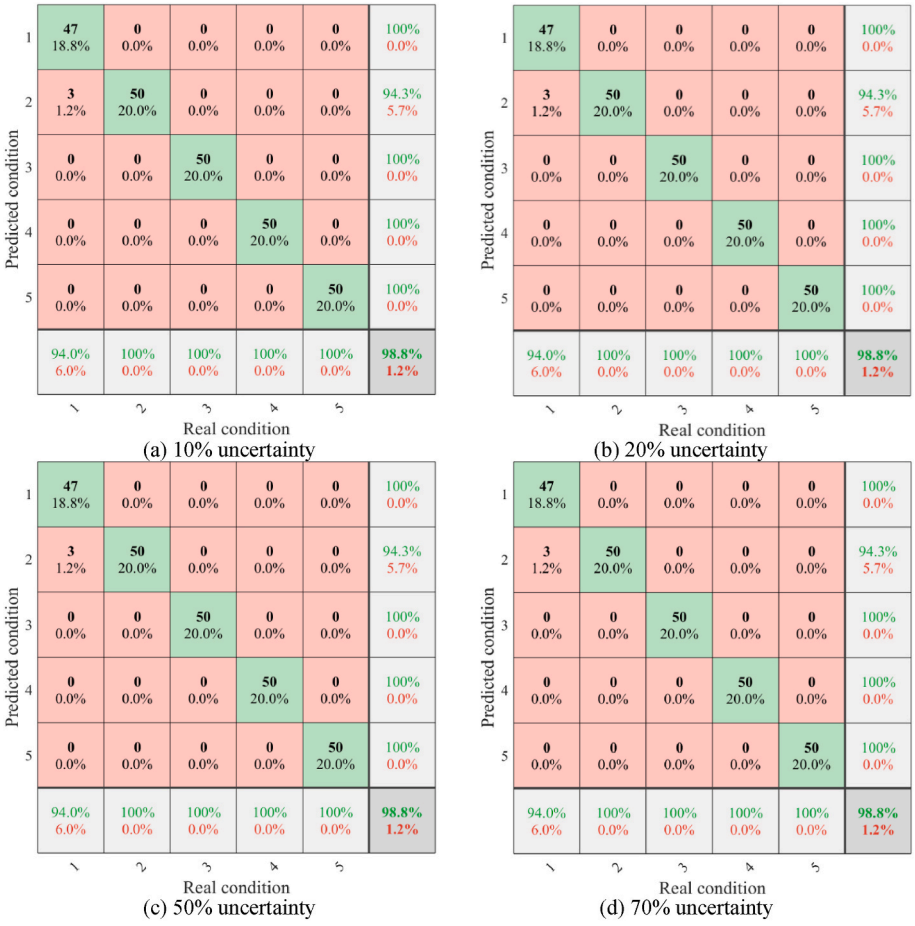

Fig. 19. Confusion matrices of prediction results of scenario SDS−1 considering different levels of uncertainties.

responses) were used as the training samples to develop the DSAE model. For other five impact locations, 10 hammer hits were executed for each impact location and each condition scenario, and the corresponding responses were employed as the validation samples to evaluate the performance of the trained model. Accordingly, 1000 groups of data were collected in total for each sensor, and a total of 15,000 groups of data were obtained for all 15 accelerometers. The ratio of training samples to validation samples is 3:1 (750/250), which meets the conventional design for machine learning research.

Fig. 10 demonstrates the influence of damage severity on the frequency response of the specimen. It is noticeable that the FFT responses of the structure are similar for all the condition scenarios. Table 2 lists the first six natural frequencies of all condition scenarios as well as the rates of change (ROC) in the natural frequencies of the four damage cases compared to the intact one when the impact location is IL1. The frequency changes of the four damage scenarios are relatively small (<1%), including that the natural frequencies are insensitive to the damage.

5. Results and discussions

5.1. Optimization and fusion results

As aforementioned, a whitening procedure based on PCA is applied to the original frequency responses to diminish the data dimensionality to benefit the model training and eliminate the noise influence. In this study, the original frequency responses of the dimension of 4000 are replaced with fewer principal components (PCs), which are subsequently employed as the inputs of the DSAE model. Fig. 11 demonstrates an example of PCA results of FFTs of vibration signals from accelerometer A1. For all the sensors, the first 200 PCs contain over 99.99% of overall information from measured vibration signals, so the input size of the DSAE model is selected as 200. A comparison of correlation coefficient matrix between original FFT responses and PCs is presented in Fig. 12, in the form of heatmap. It is clearly seen that the correlation coefficients of some FFT responses are very high, which indicates the redundant information in FFT responses. After PCA, the redundant information existing in structural responses has been significantly eliminated, and the reduced dimension of input variables is also beneficial to the model training. Since there are five condition scenarios in this study, output variables of the model are defined as (1,0,0,0,0), (0,1,0,0,0), (0,0,1,0,0), (0,0,0,1,0), and (0,0,0,0,1), corresponding to the conditions of intact, small damage, medium damage, large damage and severe damage, respectively. In addition to determination of input and output layers, the selection of hidden layers is of great importance to the generalisation capacity of the developed model. In the network design, three hidden layers with a dimension reduction configuration are considered, as suggested in (Lu et al., 2017). The values of meta-parameters, such as dropout fraction coefficient df, weight penalty factor λ, learning rate lr and neuron numbers of different hidden layers $HLN1$, $HLN2$ and $HLN3$, are optimized by the proposed EWOA during the model training. The ranges of parameters to be optimized are $df \in [0.1, 0.9]$, $\lambda \in [0.1, 0.9]$, $lr \in [0.001, 1]$, $HLN1 \in [80, 120]$, $HLN2 \in [40, 60]$ and $HLN3 \in [10, 30]$. The parameters of EWOA are set as: whale swarm size $N_p = 30$, maximum iteration number $N_{max} = 100$, minimum inertia weight $iw_{min} = 0.1$, maximum inertia weight $iw_{max} = 0.9$, and $a_0 = b = 1$. Since there are 15 accelerometers in the system, a total of 15 corresponding optimized DSAE models are developed for structural condition diagnosis, denoted by EWOA−DSAE−i ($i = 1, 2, \ldots, 15$).

Fig. 13 shows the optimization procedure of meta-parameters of

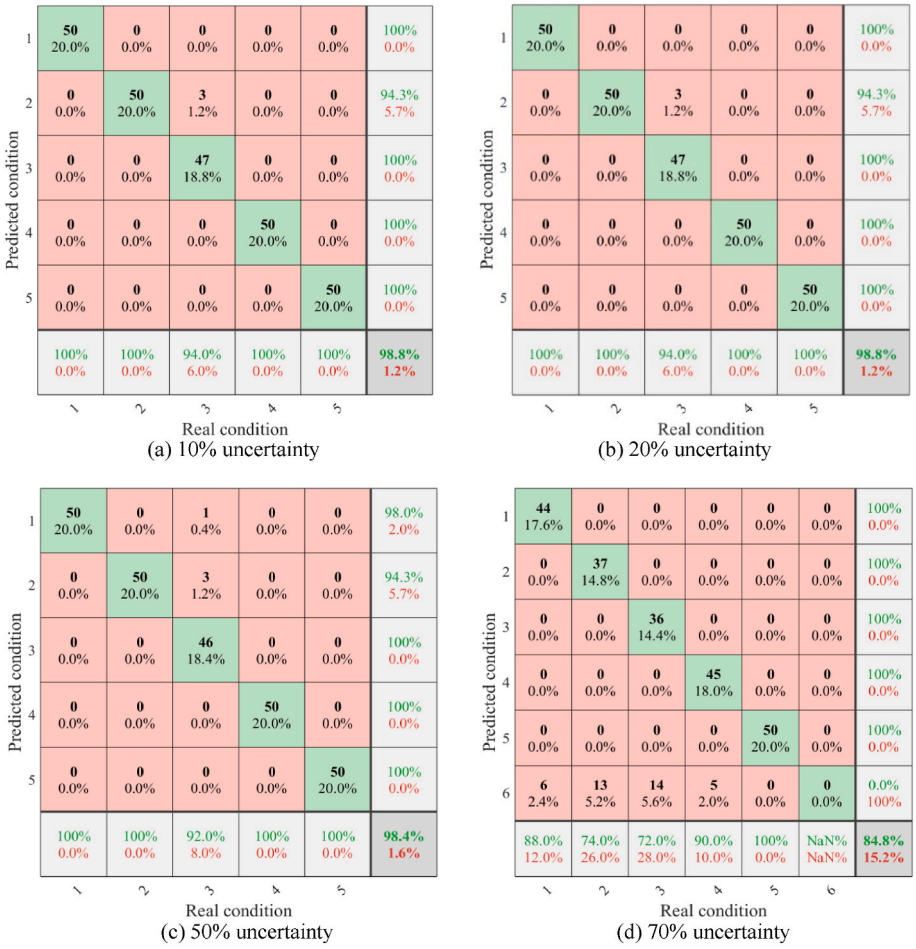

Fig. 20. Confusion matrices of prediction results of scenario SDS−2 considering different levels of uncertainties.

model EWOA−DSAE−1, which is obtained based on the data collected from accelerometer A1. The six parameters reach their optimum at around 21st iteration, indicating a fast convergence of the proposed EWOA. To further verify the superiority of the proposed algorithm in optimizing meta-parameters of DSAE models, the EWOA is compared to the standard WOA and commonly used particle swarm optimization (PSO) algorithm in terms of the prediction error of the training data from sensor A1. To make an impartial evaluation, the swarm size and maximum iteration number of WOA and PSO are set the same as that of the proposed EWOA. For other parameters of PSO, two learning coefficients are set as 1.5 and a linearly decreasing inertia weight is adopted with the minimum and maximum weight values of 0.1 and 0.9, respectively. Fig. 14 compares results of the three algorithms. Despite the fastest convergence, the PSO has the worst prediction among three algorithms, indicating the premature of the algorithm. The proposed EWOA outperforms the standard WOA in terms of both accuracy and convergence, showing its promising prospect for meta-parameter optimization of the DSAE model.

Moreover, to demonstrate the proposed EWOA−DSAE model in hierarchical feature extraction, the initial input and outputs of different hidden layers are visualised and compared using the 3-D t-distributed stochastic neighbour embedding (t-SNE) method (Hinton and Roweis, 2002). Fig. 15 shows the visualization results based on the data measured from accelerometer A1. It is hard to distinguish the structural condition in the input layer, since different colours of data points are mixed together. Even though the data points of same class start to concentrate after the 1st hidden layer, misidentification of structural condition stills exists. The features corresponding to different condition scenarios are well separated after the 2nd hidden layer, and thoroughly scattered after the 3rd hidden layer. Hence, the proposed model has outstanding feature extraction capacity and clustering performance for processing vibration signals under different conditions.

The proposed EWOA−DSAE is then compared to other three learning methods using the same data from accelerometer A1. The comparative models include EWOA−DSAE−1, standard DSAE with constant pre-set meta-parameters, 1D convolutional neural networks (CNN) and support vector machine (SVM). The standard DSAE also adopts the 5-layer network architecture including one input layer, one output layer and three hidden layers. The parameters of the standard DSAE are set as: the 1st, 2nd and 3rd hidden layers have 100, 50, 20 neurons, respectively; the learning rate is 0.1; the dropout fraction coefficient is s 0.5; the weight penalty factor is 0.5; and other parameters are the same as those of EWOA−DSAE model. The 1D-CNN model adopts 5-layer configuration including the input layer, output layer, one convolutional layer with a filter size of 3 and filter number of 16, followed by two fully connected layers with 300 neurons. In this model, batch normalisation and dropout operation are utilized after the convolutional layer to balance the model training and reduce the overfitting potential, respectively. For the SVM model, the radial basis function (RBF) is selected as the kernel to transform the original inputs into high-dimensional nonlinear space. The parameters of SVM are given as follows: the penalty factor is set as 10, and the kernel parameter is set as 2. Since the standard SVM is not supportive of resolving multi-classification problems, the one versus rest (OVR) strategy is employed to convert the multi-category classification problem into a multiple-binary classification problem. Here, five sub-SVM classifiers are developed and the voting method is applied to make the final decision.

In this comparative study, the performances of four statistical

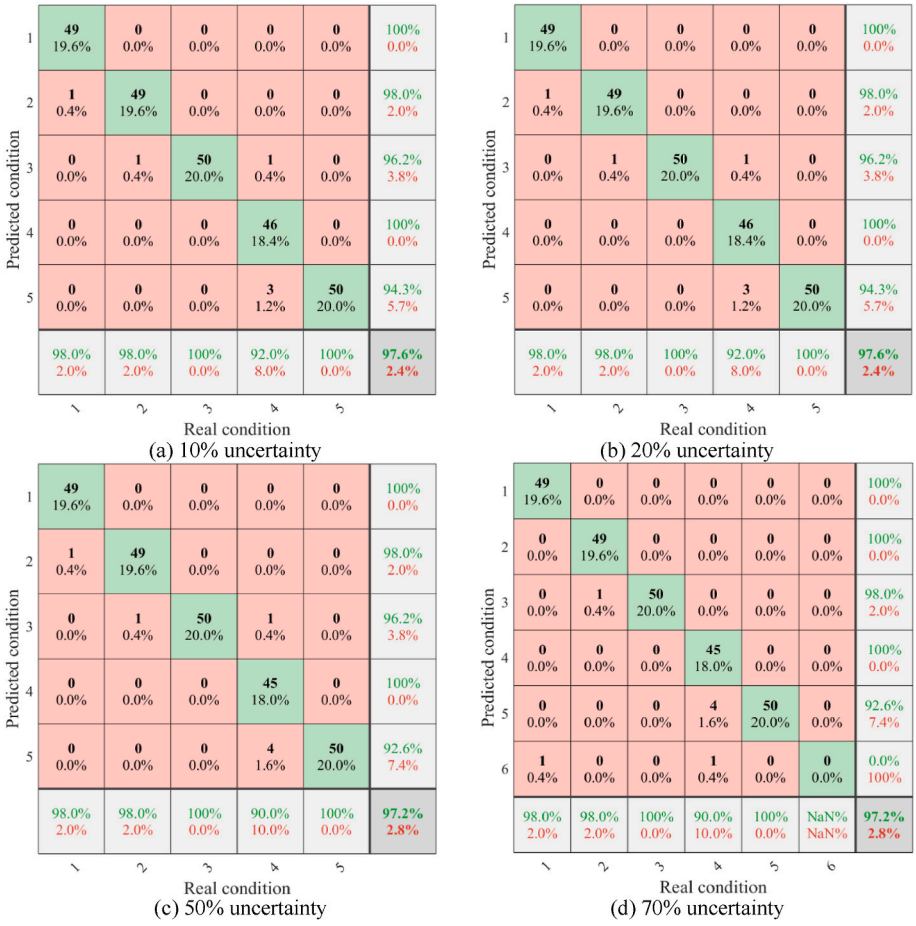

Fig. 21. Confusion matrices of prediction results of scenario SDS−3 considering different levels of uncertainties.

learning models are evaluated based on the validation samples and reported in terms of the confusion matrix, which provides the counts and percentages of true positive (TP), true negative (TN), false positive (FP) and false negative (FN) of the predicted condition classes compared to real ones. Fig. 12 displays the results of the four learning models, in which the condition labels "1", "2", "3", "4" and "5" represent the condition scenarios "intact", "small damage", "moderate damage", "large damage" and "severe damage", respectively. The overall accuracy of the validation samples predicted by the proposed EWOA−DSAE model is 94.4%, which is higher than those of DSAE, CNN and SVM models. In detail, for the EWOA−DSAE model, six intact cases are wrongly recognised as small damage cases; three small damage cases are wrongly identified as either intact (1) or moderate damage cases (2); five large damage cases are inaccurately identified as severe damage cases; all moderate damage and severe damage cases are accurately predicted. Only one damage case is incorrectly identified as intact condition, with 0.5% false positive. However, for the DSAE model, more damaged cases are recognised as intact ones. In addition, although the 1D CNN and SVM have high capacity to distinguish damaged cases from intact ones, they fail to evaluate the damage severity. For instance, 11 large damage cases are wrongly predicted by the 1D CNN model and 12 moderate damage cases are inaccurately evaluated by the SVM model.

Besides, several statistical evaluation indicators are defined for quantifying the performance of these models. The existing indicators are mainly used for evaluating the models for binary classification. Consequently, we consider the multi-class classification as multiple binary classifications and calculate the averaged values of these indicators, including averaged accuracy, averaged macro-F_1 and averaged micro-F_1. The detailed mathematical expressions of three indicators are displayed in Eqs. (20)-(22)

$$Accuracy = \frac{\sum_{i=1}^{N_{cl}} (TP_i + TN_i)}{\sum_{i=1}^{N_{cl}} (TP_i + FP_i + FN_i + TN_i)} \tag{20}$$

$$Macro - F_1 = \frac{2 \bullet \frac{1}{N_{cl}} \sum_{i=1}^{N_{cl}} \frac{TP_i}{TP_i + FP_i} \bullet \frac{1}{N_{cl}} \sum_{i=1}^{N_{cl}} \frac{TP_i}{TP_i + FN_i}}{\frac{1}{N_{cl}} \sum_{i=1}^{N_{cl}} \frac{TP_i}{TP_i + FP_i} + \frac{1}{N_{cl}} \sum_{i=1}^{N_{cl}} \frac{TP_i}{TP_i + FN_i}} \tag{21}$$

$$Micro - F_1 = \frac{2 \bullet \frac{\sum_{i=1}^{N_{cl}} TP_i}{\sum_{i=1}^{N_{cl}} (TP_i + FP_i)} \bullet \frac{\sum_{i=1}^{N_{cl}} TP_i}{\sum_{i=1}^{N_{cl}} (TP_i + FN_i)}}{\frac{\sum_{i=1}^{N_{cl}} TP_i}{\sum_{i=1}^{N_{cl}} (TP_i + FP_i)} + \frac{\sum_{i=1}^{N_{cl}} TP_i}{\sum_{i=1}^{N_{cl}} (TP_i + FN_i)}} \tag{22}$$

where N_{cl} denotes the number of structural condition scenarios, which is $N_{cl} = 5$ in this study. Table 3 summarises the statistical evaluation results of these four models. As compared with the other three models, the proposed model has the highest performance indicators, namely, 0.9776 for the averaged accuracy, 0.9455 for the averaged macro-F_1, and 0.9440 for averaged micro-F_1. The evaluation results in Fig. 16 and Table 3 demonstrate that the proposed EWOA-DSAE is the best one in condition scenario classification and severity estimation among four models.

In the same way, the EWOA-DSAE models corresponding to accelerometers A2 to A15 are developed using the training data and then

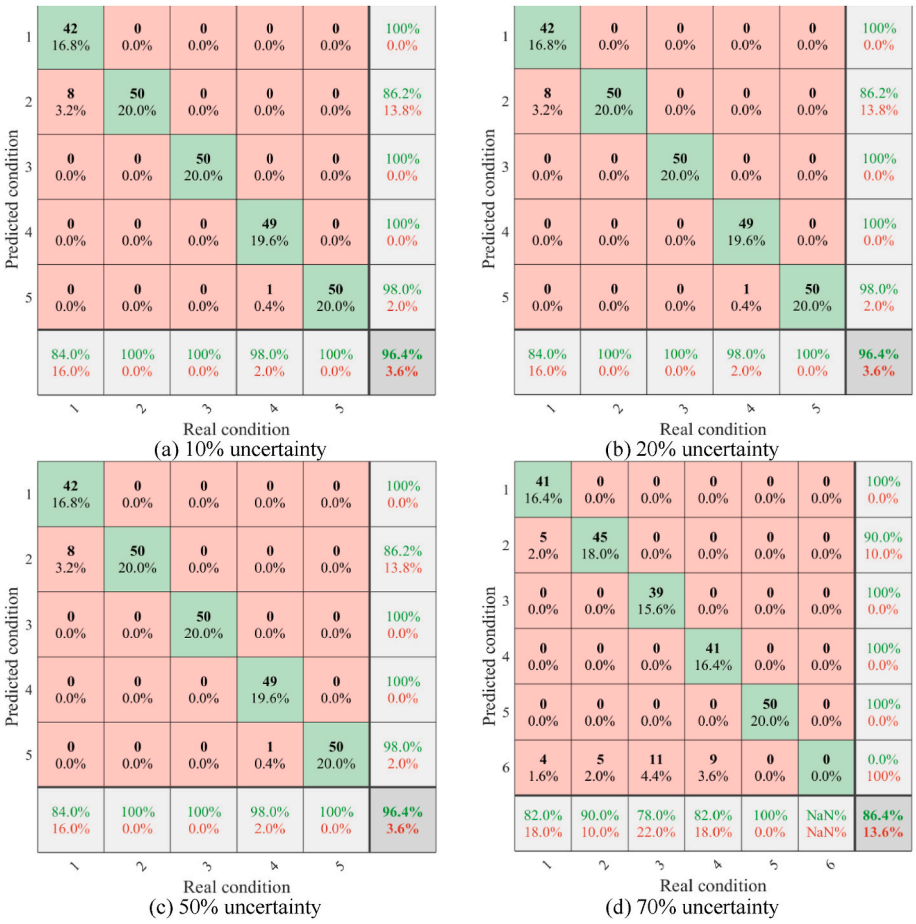

Fig. 22. Confusion matrices of prediction results of scenario SDS−4 considering different levels of uncertainties.

evaluated using the validation data. Table 4 summarises the identification accuracies of all 15 optimized DSAE models for training, validation and overall data samples. Most models have satisfactory prediction performance (>90%) for the training samples, except EWOA−DSAE−2, EWOA−DSAE−4, EWOA−DSAE−6, EWOA−DSAE−10 and EWOA−DSAE−11. The main reason for the low performance is that the corresponding accelerometers are perhaps affected by either the deployment location or sensor fault, which further influences the quality of measured data and training accuracy of the developed models. To address this problem, the D-S algorithm is utilized to fuse the outputs of 15 EWOA-DSAE models to gain the final result. Here, ε_1 and ε_2 in the D-S decision criteria are respectively set to 0.1 and 0.2 to guarantee that the confidence of the correct proposition is obviously higher than that of other propositions in frame of discernment.

Tables 5 and 6 provide an example of small damage case (CS1) to show how the EWOA-DSAE predictions are fused for the final decision. In Table 5, m_i (i = 1, 2, …, 15) denotes the PA of the ith evidence, corresponding to the probabilistic output of the ith EWOA-DSAE model (EWOA−DSAE−i), and CS1−CS5 represent the five condition scenarios. The second evidence (m_2), obtained from model EWOA−DSAE−2 corresponding to accelerometer A2, assigns more PA (confidence) to the condition scenario "intact" (0.7539) than "small damage" (0.2245), which is real structural condition. The same problem happens at sensors A8 and A13, in which the prediction outcome is "intact" rather than the real condition "small damage". In addition, accelerometer A4 is hard to make the prediction, since the decision criteria is not satisfied due to the close PAs of propositions "intact" and "small damage". Hence, if only one sensor or limited sensors are deployed to evaluate the structural condition, the diagnostic system either makes the wrong prediction or is difficult to make the prediction confidently.

Table 6 shows the decision result of combing the predictions of 15 accelerometers by the D-S algorithm. Using the multi-sensor fusion, the PA of correct proposition "small damage" has increased to 1, while the PAs of other propositions declines to 0, demonstrating a high confidence level. Fig. 17 portrays the confusion matrix of predictions of all the validation samples after data fusion. It is apparent that all samples are correctly predicted and the accuracy of proposed method can reach 100%, demonstrating the promising potential in practical applications.

5.2. *Influence of sensor deployment on performance of proposed approach*

In the real situation, it is difficult to install so many accelerometers to monitor such a structural component due to the installation availability and economic consideration. Besides, the damage location is unknown beforehand in most circumstances. As a result, it is necessary to investigate the influences of number and location of deployed accelerometers on the prediction performance of the proposed method. In this section, five sensor deployment scenarios are considered with detailed descriptions as follows.

- Sensor deployment scenario 1 (SDS−1): All the accelerometers are included.
- Sensor deployment scenario 2 (SDS−2): Accelerometers A2, A3 and A9 are included, which are installed close to real damage location.
- Sensor deployment scenario 3 (SDS−3): Accelerometers A5, A6, A7 and A8 are included, which are installed far from real damage location.

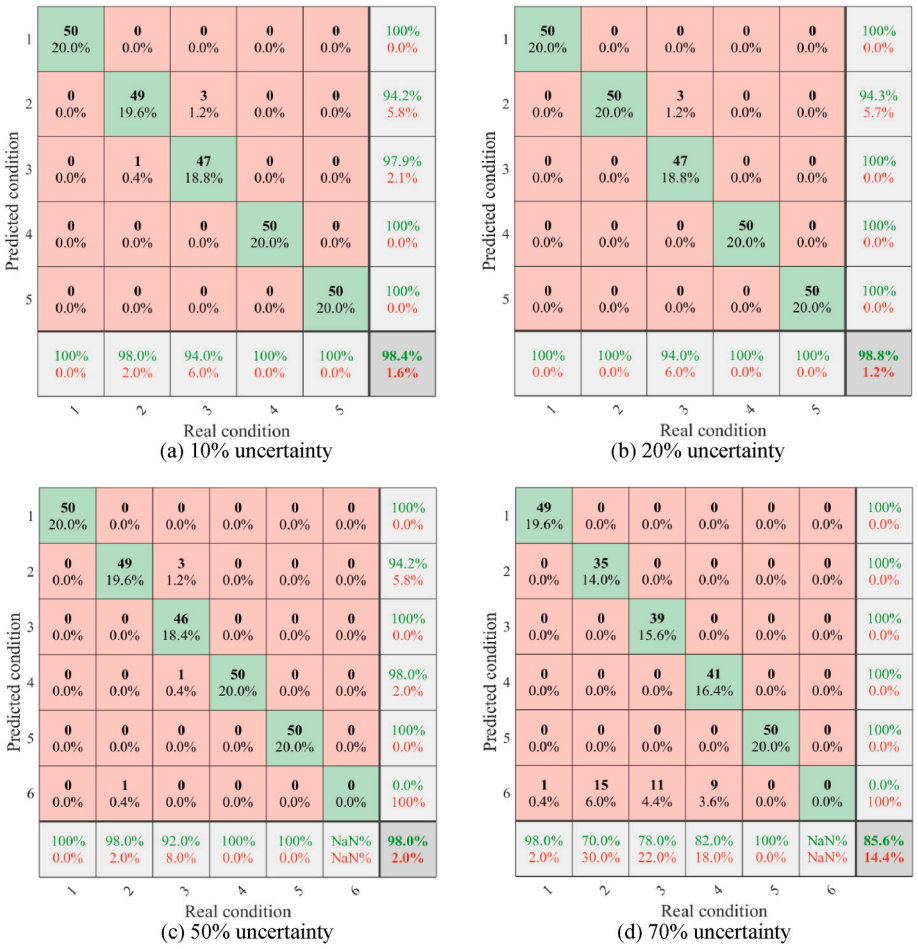

Fig. 23. Confusion matrices of prediction results of scenario SDS−5 considering different levels of uncertainties.

- Sensor deployment scenario 4 (SDS−4): Accelerometers A1, A2 and A10 are included, which are installed on the left of real damage location.
- Sensor deployment scenario 5 (SDS−5): Accelerometers A3, A4 and A9 are included, which are installed on the right of real damage location.

Fig. 18 demonstrates confusion matrices of model predictions of scenarios SDS−2, SDS−3, SDS−4 and SDS−5, respectively. It is clearly observed that the proposed optimized deep learning models with multi-sensor fusion algorithm is capable of accurately diagnosing the progressive damage, even if only limited number of accelerometers are deployed in the system. The accuracies of four scenarios for diagnosing the validation samples are 98.8%, 98.8%, 96.4% and 98.4%, respectively. For SDS−2, all the intact cases are accurately diagnosed, and only three moderate damage cases are wrongly recognised as the small damage cases. Moreover, only 3, 9 and 4 cases are falsely predicted for SDS−3, SDS−4 and SDS−5, respectively. A promising phenomenon can be found that none of damaged cases are identified as intact, which is of great importance for using the proposed method for damage detection of real structures. Table 7 displays the results of three statistical evaluation indicators of models developed for all five sensor deployment scenarios. The best performance is gained for Scenario SDS−1, in which all the accelerometers are considered for damage diagnosis. Except SDS−1, the SDS−2 has the optimal performance with evaluation indicators of 0.9952 of accuracy, 0.9883 of Macro-F_1 and 0.9880 of Micro-F_1, where only three sensors are considered in the system. The main reason for this result is that three sensors are deployed in the immediate area of the damage. Even though the SDS−3 has four sensors installed far from the damage location, it has better evaluation results than SDS−4 and SDS−5, where three sensors are deployed on the left and ride sides of damage, respectively. Consequently, the number of accelerometers is more crucial than the sensor deployment location, because the diagnosis accuracy can be enhanced by multi-sensor fusion.

5.3. *Influence of uncertainty level on performance of proposed approach in damage detection*

It should be worth noting that in above analysis, the probabilistic outputs of EWOA−DSAE models are directly regarded as the probabilistic assignments in D-S algorithm fusion, which indicates that the uncertainty in frame of discernment (Θ) is 0. However, in the real world, uncertainty always exists in the structural dynamics, due to inherent variabilities of geometric and material properties as well as unmodeled physics, which could not be neglected. Hence, in this section, the influence of uncertainty on damage identification of the proposed method is studied. Both low and high levels of uncertainty are considered in this investigation, i.e. 10%, 20%, 50% and 70%. Suppose the uncertainty level is denoted by *ul*, the probabilistic assignments of elements in frame of discernment can be rewritten as:

$$\begin{aligned} m^*(D_i) &= (1-ul) \bullet m(D_i), i = 1, 2, \ldots, 5 \\ m^*(\Theta) &= ul \end{aligned} \tag{23}$$

where $m(D_i)$ (i = 1, 2, …, 5) denotes the PA of ith condition scenario without considering the uncertainty, which equals to the probabilistic output of EWOA-DSAE model; $m^*(D_i)$ denotes the PA of ith condition scenario when the uncertainty level is *ul*.

Table 8 provides an example of PAs of a large damage case under the scenario SDS−2, when the uncertainty level is 50%. In this scenario, only three accelerometers (A2, A3 and A9) are considered in the system for structural damage diagnosis. From the PAs of condition scenarios in the frame of discernment, the uncertainty (Θ) occupies the maximum PA for all three pieces of evidence, which means that it is very hard for the system to make the decision and the condition diagnosis result is "uncertain". Furthermore, in m_2^*, the focal element D5 (severe damage) has higher value of PA than real condition (D4), which indicates that the diagnosis result is more inclined to "severe damage" than "large damage" regardless of the influence of uncertainty. After fusing three pieces of evidence, the PA of correct proposition (D4: large damage) has increased to 0.7265, which is much higher than the PAs of other condition scenarios, as shown in Table 9. In the meantime, the uncertainty has decreased from 0.5 to 0.1649.

Figs. 19–23 depict the confusion matrices of model predictions of all the sensor deployment scenarios considering different levels of uncertainty. From the results of scenario SDS−1 in Fig. 19, it is clearly seen that the system can guarantee the high accuracy (98.8%) of validation case prediction for all the uncertainty levels. The main reason for this phenomenon is that in this deployment scenario, all 15 accelerometers are included for making the diagnosis and the uncertainty can be gradually eliminated via fusing all the sensor predictions despite of high uncertainty level. From the results of scenario SDS−2 in Fig. 20, the proposed approach also exhibits outstanding performance with the prediction accuracy of higher than 98%, except the case of 70% uncertainty level. It should be noted that in Fig. 20 (d) a new label "6" appears in the confusion matrix, indicating the condition status of "uncertain". It can be seen that for the scenario SDS−2, there are 6 intact cases, 13 small damage cases, 14 moderate damage cases and 5 large damage cases identified as "uncertain", when the uncertainty level is as high as 70%. The major reason leading to this embarrassed outcome is due to high uncertainty level and limited sensors (A2, A3 and A9) in scenario SDS−2. Though the PA of uncertainty in frame of discernment can be diminished via the fusion operation, the fused result still contains higher PA in "uncertain" than other condition scenarios in frame of discernment because of fewer pieces of evidence (m_i^*), causing the decision system difficult to make a final diagnosis. Therefore, as aforementioned, the number of sensors is more important than the sensor location in the proposed method, since more sensors indicates more evidences for data fusion to reduce the uncertainty. This point can be well proved by comparing the results in Figs. 20 (d) and Fig. 21 (d), which is the confusion matrix for scenario SDS−3 under 70% uncertainty level. Compared to SDS−2, SDS−3 has one more sensor in the system, but four accelerometers in SDS−3 are located far away from the damage location. From the confusion matrices of both scenarios under 70% uncertainty level, the model for SDS−2 has the accuracy of 84.8% with 38 cases identified as "uncertain" while the model for SDS−3 possesses higher accuracy of 97.2% with only 2 cases identified as "uncertain". This comparative result is very promising for the application of proposed method in the field, because in real situations we do not know the damage location in advance. The results of scenarios SDS−4 and SDS−5 are similar to that of SDS−2. At the uncertainty levels of 10%, 20% and 50%, the models corresponding to both scenarios can ensure high prediction accuracy of above 96%. However, at the uncertainty level of 70%, the prediction accuracies for scenarios SDS−4 and SDS−5 are decreased to 86.4% and 85.6%, respectively, with several cases diagnosed as "uncertain". On the whole, combing the results of all the condition scenarios, it can be concluded that multi-sensor fusion is capable of effectively increasing the PA of correct proposition and lowering the uncertainty, which makes it the system easy to make a correct final decision.

6. Conclusions

This study develops a novel structural damage diagnosis framework by integrating PCA, DSAE, EWOA and D-S fusion techniques. The PCA eliminates noise and diminishes the dimension of the frequency domain data. The DSAE establishes a statistical DL model to predict the structural condition. The EWOA is developed to find optimal meta-parameters of DSAE during the training process. The D-S evidence theory is utilized to combine the results from individual sensors to obtain an integrated diagnosis result. The developed framework is applied to a laboratory-tested beam model. The following conclusions can be drawn:

- The developed EWOA introduces self-adaptive inertia weight and symmetric spiral curve path to improve search ability and avoid falling into local optimum. It outperforms the standard WOA and PSO in terms of optimization of meta-parameters of DSAE for structural damage diagnosis.
- The proposed EWOA-DSAE, with self-adaptive optimization of model parameters, has higher diagnostic accuracy than the 1D CNN, SVM and standard DSAE models.
- Combination of EWOA-DSAE and multi-sensor fusion algorithm is able to improve the diagnosis accuracy and enhance the confidence degree of diagnosis result, even under the condition of limited sensors and high uncertainty level.

Even though the proposed framework has been proven to be effective in damage diagnosis of concrete arch beam with higher accuracy and confidence degree, there exists some limitations and disadvantages that hinder its real application. For instance, the framework in this study is mainly developed for concrete jack arch beam. However, in practice, a generalised method/framework that can be used to deal with different types of structures is preferable. Hence, whether it works for other types of civil structures needs further investigation. In addition, this study only considers the most vulnerable damage location. In real situations, structural damages may occur at different locations, and even multiple damages may exist simultaneously in the same structure. Accordingly, damage localisation is also a challenging task that needs to be addressed for practical implementation of the proposed framework. In future work, different types of structural models will be designed and fabricated in the laboratory. The proposed framework will be evaluated based on these models with the introduction of artificial damages of different locations and severities. Furthermore, transfer learning technology will be employed to transfer the proposed framework in this study, designed for damage detection of concrete jack arch beam, to the one that can be used for different types of structures to identify damage.

Declaration of competing interest

The authors declare that they have no known competing financial interests or personal relationships that could have appeared to influence the work reported in this paper.

Data availability

Data will be made available on request.

Acknowledgements

This research was supported by Australian Research Council (Grant No. LP110200162) and National Natural Science Foundation of China (Grant No. 52108288). The authors acknowledge the financial support from funding bodies for this research. Additionally, Dr Van Vu Nguyen is appreciated for the assistance in design and experimental test of the specimen in the laboratory.

Appendix

To assess the performance of the proposed EWOA in solving the optimization problems, a numerical investigation is conducted via comparison with other homogeneous heuristic algorithms (WOA and PSO) with regard to the solution error and convergence speed. The comparison is conducted based on 9 commonly used benchmark functions consisting of both unimodal and multi-modal nonlinear functions, the detailed information of which are shown in Table A1, including expression, parameter dimension and range, and expected value. A 2-D diagrammatic representation of 9 test functions is displayed in Fig. A1.

Table A.1
Details of test functions

Index	Expression of function	Dimension	Range	Result
TF1	$f(x) = \sum_{i=1}^{n} x_i^2$	30	[-100,100]	0
TF2	$f(x) = \sum_{i=1}^{n} \lvert x_i \rvert + \prod_{i=1}^{n} \lvert x_i \rvert$	30	[-10,10]	0
TF3	$f(x) = \sum_{i=1}^{n} i x_i^4 + random[0,1)$	30	[-1.28,1.28]	0
TF4	$f(x) = \sum_{i=1}^{D-1} [100(x_{i+1} - x_i^2)^2 + (x_i - 1)^2]$	30	[-30,30]	0
TF5	$f(x) = \sum_{i=1}^{n} \lvert x_i \sin(x_i) + 0.1 x_i \rvert$	30	[-10,10]	0
TF6	$f_6(x) = -20e^{\left[-0.2\sqrt{\frac{1}{n}\sum_{i=1}^{n} x_i^2}\right]} - e^{\left(\frac{1}{n}\sum_{i=1}^{n}\cos(2\pi x_i)\right)} + 20 + e$	30	[-32,32]	0
TF7	$f_7(x) = 0.1\{\sin^2(3\pi x_1) + \sum_{i=1}^{n}(x_i - 1)^2[1 + \sin^2(3\pi x_i + 1)] + (x_n - 1)^2[1 + \sin^2(3\pi x_n)]\} + \sum_{i=1}^{n} u(x_i, 5, 100, 4)$ $u(x_i, a, k, m) = \begin{cases} k(x_i - a)^m, x_i > a \\ 0, -a < x_i < a \\ k(-x_i - a)^m, x_i < -a \end{cases}$	30	[-50,50]	0
TF8	$f_8(x) = \frac{1}{4000}\sum_{i=1}^{n} x_i^2 - \prod_{i=1}^{n} \cos\left(\frac{x_i}{\sqrt{i}}\right) + 1$	30	[-600,600]	0
TF9	$f_9(x) = \sum_{i=1}^{n} [x_i^2 - 10\cos(2\pi x_i) + 10]$	30	[-5.12,5.12]	0

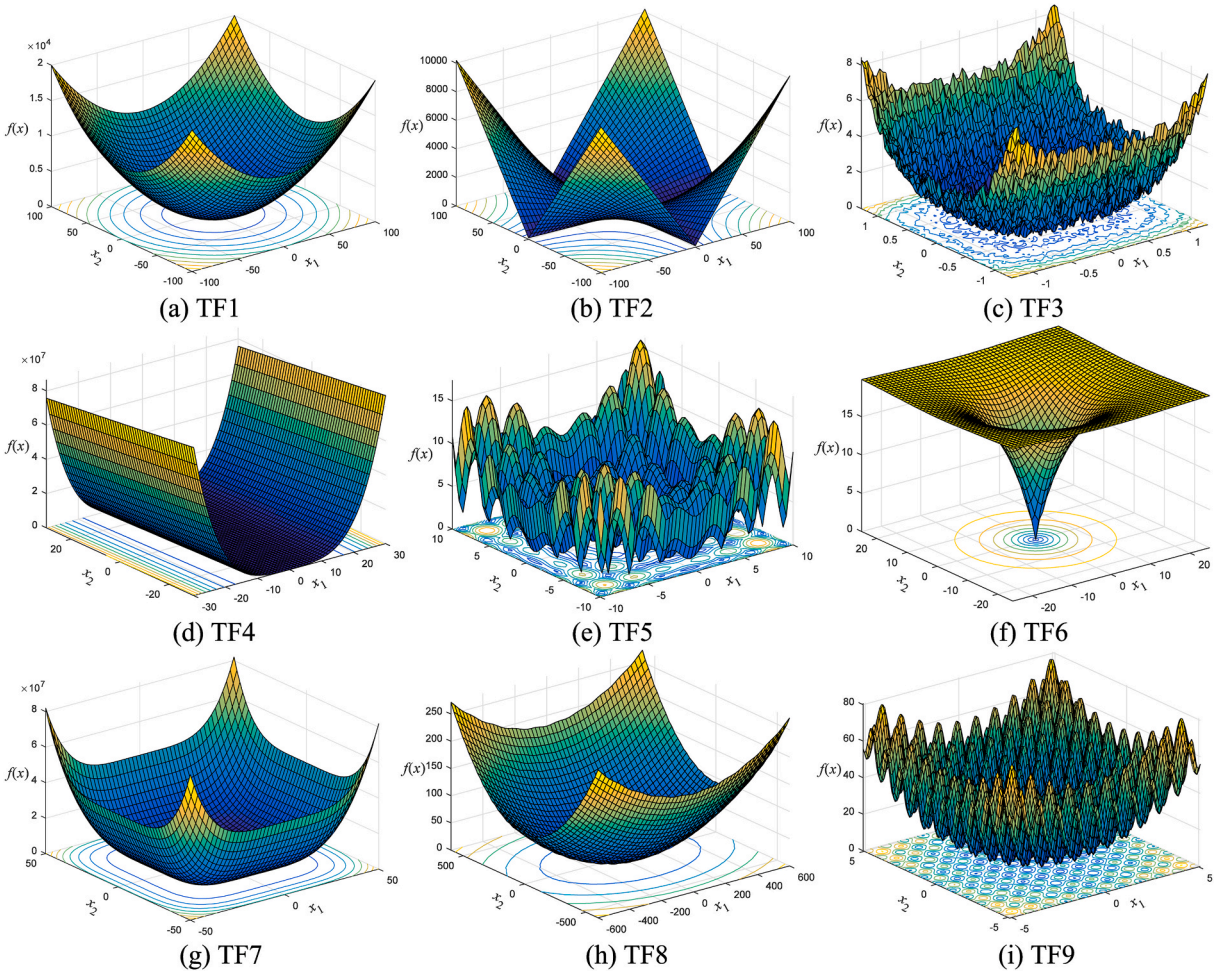

Fig. A.1. 2-D diagrammatic representation of test functions.

Table A2 summarises the comparison results of three optimization

algorithms, in terms of maximum, minimum and averaged fitness values as well as standard deviation. It is clearly seen that the proposed EWOA has the optimal fitness values among three algorithms for all the cases. Even if EWOA has the optimization result of TF4 with apparent deviation from the expected value, it is superior to WOA and PSO in the evaluation indices. Accordingly, considering all the fitness results, it can be concluded that the proposed EWOA is more effective in solving optimization problems than the other two algorithms.

Table A.2
Optimization results of test functions using different algorithms.

Function	Method	Maximum fitness	Minimum fitness	Averaged fitness	Standard deviation
TF1	PSO	8.56e-05	2.32e-14	1.84e-06	1.21e-05
	WOA	1.74e-70	1.30e-72	3.49e-72	2.46e-71
	EWOA	0	0	0	0
TF2	PSO	3.54e-12	6.44e-15	3.19e-13	6.28e-13
	WOA	7.83e-47	5.03e-56	2.15e-48	1.16e-47
	EWOA	0	0	0	0
TF3	PSO	10.1004	0.0156	1.6869	2.2314
	WOA	0.0306	5.11e-05	0.0044	0.0058
	EWOA	3.28e-04	3.85e-07	8.36e-05	8.77e-05
TF4	PSO	1.66e+07	47.9918	1.38e+06	2.95e+06
	WOA	48.6844	47.2097	48.1551	0.4268
	EWOA	48.5710	0.0014	40.7742	17.9292
TF5	PSO	178.9664	1.01e-14	62.8482	69.2822
	WOA	6.91e-49	3.32e-58	1.82e-50	9.84e-50
	EWOA	0	0	0	0
TF6	PSO	4.8359	7.52e-08	0.0978	0.6837
	WOA	7.99e-15	8.88e-16	4.37e-15	2.73e-15
	EWOA	8.88e-16	8.88e-16	8.88e-16	0
TF7	PSO	7.01e+07	4.2102	8.36e+06	1.31e+07
	WOA	2.2355	0.2688	1.2189	0.5295
	EWOA	0.2814	4.08e-06	0.0314	0.0523
TF8	PSO	0.6239	5.51e-14	0.0532	0.1514
	WOA	0.2517	0	0.0093	0.0463
	EWOA	0	0	0	0
TF9	PSO	39.8748	0	1.5033	6.3539
	WOA	1.14e-13	0	2.27e-15	1.61e-14
	EWOA	0	0	0	0

Fig. A2 compares the convergences and accuracies of three algorithms in optimizing all the test functions. It is obvious that the PSO has better convergence than WOA and EWOA in most cases. However, it falls into the local optimal solutions for the functions of TF1, TF2, TF3, TF5 and TF9. The proposed EWOA, with a little lower convergence rate, has the best optimization accuracy for all nine functions.

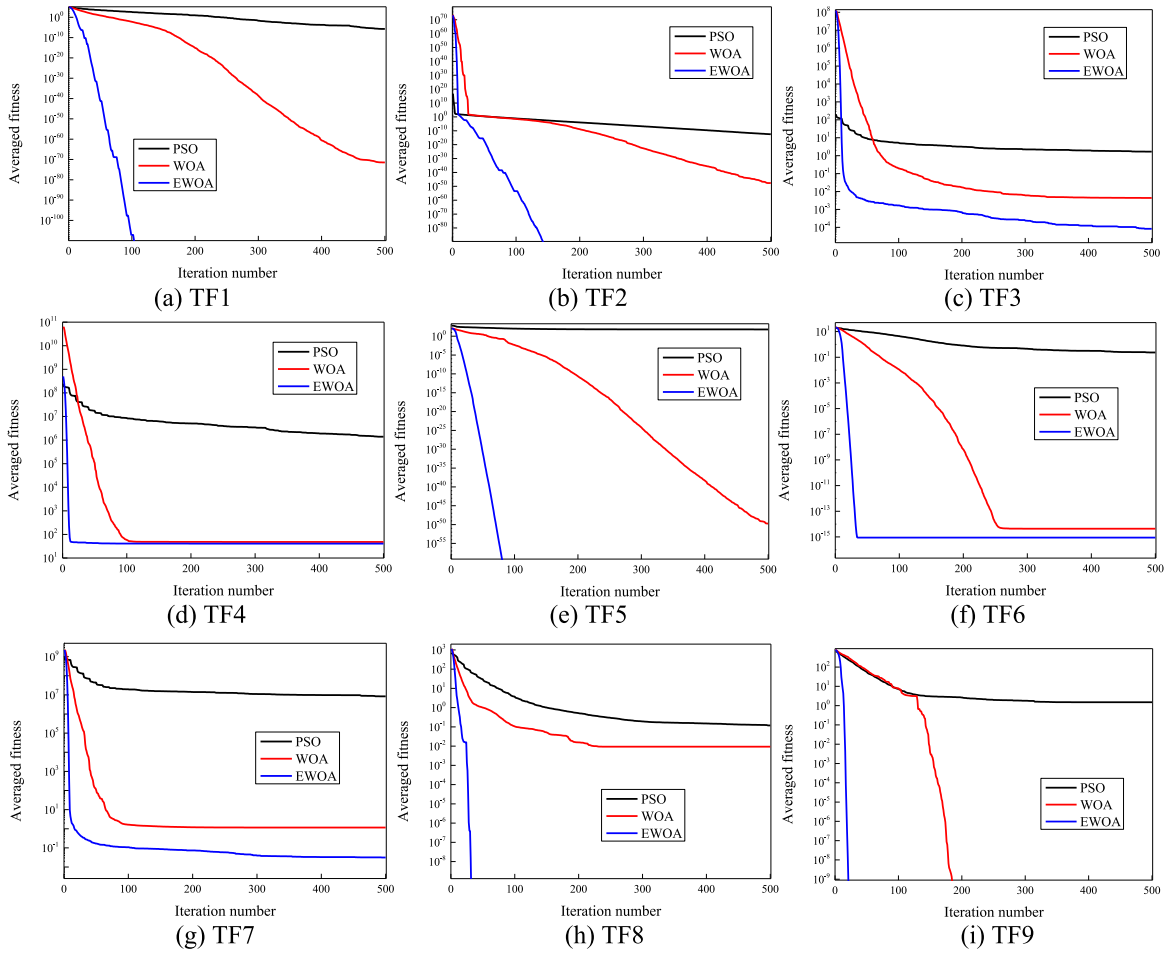

Fig. A.2. Convergence comparison of different optimization algorithms.

References

Ai, D., Mo, F., Yang, F., Zhu, H., 2022. Electromechanical impedance-based concrete structural damage detection using principal component analysis incorporated with neural network. J. Intell. Mater. Syst. Struct. 33, 2241–2256.

Avci, O., Abdeljaber, O., Kiranyaz, S., Hussein, M., Gabbouj, M., Inman, D.J., 2021. A review of vibration-based damage detection in civil structures: from traditional methods to Machine Learning and Deep Learning applications. Mech. Syst. Signal Process. 147.

Bao, Y., Tang, Z., Li, H., Zhang, Y., 2019. Computer vision and deep learning–based data anomaly detection method for structural health monitoring. Struct. Health Monit. 18, 401–421.

Bao, Y., Liu, D., Tang, Z., Li, H., 2020. Machine-learning-based Methods for Output Only Structural Modal Identification arXiv preprint arXiv:2004.07644.

Caicedo, D., Lara-Valencia, L., Valencia, Y., 2022. Machine learning techniques and population-based metaheuristics for damage detection and localization through frequency and modal-based structural health monitoring: a review. Arch. Comput. Methods Eng. 29, 3541–3565.

Chen, S., Ong, Z.C., Lam, W.H., Lim, K.-S., Lai, K.W., 2020. Unsupervised damage identification scheme using PCA-reduced frequency response function and waveform chain code analysis. Int. J. Struct. Stabil. Dynam. 20, 2050091.

Dempster, A.P., 2008. Upper and Lower Probabilities Induced by a Multivalued Mapping, Classic Works of the Dempster-Shafer Theory of Belief Functions. Springer, pp. 57–72.

Dick, K., Russell, L., Souley Dosso, Y., Kwamena, F., Green, J.R., 2019. Deep learning for critical infrastructure resilience. J. Infrastruct. Syst. 25, 05019003.

Dinh-Cong, D., Truong, T.T., Nguyen-Thoi, T., 2022. A comparative study of different dynamic condensation techniques applied to multi-damage identification of FGM and FG-CNTRC plates. Eng. Comput. 38, 3951–3975.

Entezami, A., Shariatmadar, H., 2018. An unsupervised learning approach by novel damage indices in structural health monitoring for damage localization and quantification. Struct. Health Monit. 17, 325–345.

Fan, G., Li, J., Hao, H., 2019. Lost data recovery for structural health monitoring based on convolutional neural networks. Struct. Control Health Monit. 26, e2433.

Farrar, C.R., Worden, K., 2012. Structural Health Monitoring: a Machine Learning Perspective. John Wiley & Sons.

Flah, M., Nunez, I., Chaabene, W.B., Nehdi, M.L., 2020. Machine learning algorithms in civil structural health monitoring: a systematic review. Arch. Comput. Methods Eng. 1–23.

Gao, Y., Kong, B., Mosalam, K.M., 2019. Deep leaf-bootstrapping generative adversarial network for structural image data augmentation. Comput. Aided Civ. Infrastruct. Eng. 34, 755–773.

Hinton, G., Roweis, S.T., 2002. Stochastic Neighbor Embedding. NIPS, Citeseer, pp. 833–840.

Hou, R., Xia, Y., Zhou, X., 2018. Structural damage detection based on l1 regularization using natural frequencies and mode shapes. Struct. Control Health Monit. 25, e2107.

Kamariotis, A., Chatzi, E., Straub, D., 2023. A framework for quantifying the value of vibration-based structural health monitoring. Mech. Syst. Signal Process. 184, 109708.

Khayatazad, M., De Pue, L., De Waele, W., 2020. Detection of corrosion on steel structures using automated image processing. Developments in the Built Environment 3, 100022.

Kim, H., Sim, S.H., 2019. Automated peak picking using region-based convolutional neural network for operational modal analysis. Struct. Control Health Monit. 26, e2436.

Kullaa, J., 2011. Distinguishing between sensor fault, structural damage, and environmental or operational effects in structural health monitoring. Mech. Syst. Signal Process. 25, 2976–2989.

Lakshmi, D., Ponnusamy, R., 2021. Facial emotion recognition using modified HOG and LBP features with deep stacked autoencoders. Microprocess. Microsyst. 82, 103834.

Le, H.Q., Truong, T.T., Dinh-Cong, D., Nguyen-Thoi, T., 2021. A deep feed-forward neural network for damage detection in functionally graded carbon nanotube-reinforced composite plates using modal kinetic energy. Front. Struct. Civ. Eng. 15, 1453–1479.

Li, C., Xu, P., Niu, L., Chen, Y., Sheng, L., Liu, M., 2019. Tunnel crack detection using coarse-to-fine region localization and edge detection. Wiley Interdisciplinary Reviews: Data Min. Knowl. Discov. 9, e1308.

Liu, J., Huang, Y., Zou, Q., Tian, M., Wang, S., Zhao, X., Dai, P., Ren, S., 2019. Learning visual similarity for inspecting defective railway fasteners. IEEE Sensor. J. 19, 6844–6857.
Lu, C., Wang, Z.-Y., Qin, W.-L., Ma, J., 2017. Fault diagnosis of rotary machinery components using a stacked denoising autoencoder-based health state identification. Signal Process. 130, 377–388.
Lyu, T., Xu, C., Chen, G., Li, Q., Zhao, T., Zhao, Y., 2019. Health state inversion of Jack-up structure based on feature learning of damage information. Eng. Struct. 186, 131–145.
Ma, X., Lin, Y., Nie, Z., Ma, H., 2020. Structural damage identification based on unsupervised feature-extraction via Variational Auto-encoder. Measurement 160, 107811.
Mirjalili, S., Lewis, A., 2016. The whale optimization algorithm. Adv. Eng. Software 95, 51–67.
Nguyen, T., Truong, T.T., Nguyen-Thoi, T., Bui, L.V.H., Nguyen, T.-H., 2022. Evaluation of Residual Flexural Strength of Corroded Reinforced Concrete Beams Using Convolutional Long Short-Term Memory Neural Networks, Structures. Elsevier, pp. 899–912.
Pathirage, C.S.N., Li, J., Li, L., Hao, H., Liu, W., Ni, P., 2018. Structural damage identification based on autoencoder neural networks and deep learning. Eng. Struct. 172, 13–28.
Pathirage, C.S.N., Li, J., Li, L., Hao, H., Liu, W., Wang, R., 2019. Development and application of a deep learning–based sparse autoencoder framework for structural damage identification. Struct. Health Monit. 18, 103–122.
Sen, D., Aghazadeh, A., Mousavi, A., Nagarajaiah, S., Baraniuk, R., Dabak, A., 2019. Data-driven semi-supervised and supervised learning algorithms for health monitoring of pipes. Mech. Syst. Signal Process. 131, 524–537.
Shafer, G., 1976. A Mathematical Theory of Evidence. Princeton university press.
Şimşek, B., Doruk, S., Ceran, Ö.B., Uygunoğlu, T., 2021. Principal component analysis approach to dispersed graphene oxide decorated with sodium dodecyl sulfate cement pastes. J. Build. Eng., 102234
Sohn, H., 2007. Effects of environmental and operational variability on structural health monitoring. Phil. Trans. Math. Phys. Eng. Sci. 365, 539–560.
Terzis, D., 2022. Monitoring innovation metrics in construction and civil engineering: trends, drivers and laggards. Developments in the Built Environment 9, 100064.
Truong, T.T., Lee, J., Nguyen-Thoi, T., 2022a. An effective framework for real-time structural damage detection using one-dimensional convolutional gated recurrent unit neural network and high performance computing. Ocean Eng. 253, 111202.
Truong, T.T., Lee, J., Nguyen-Thoi, T., 2022b. Joint damage detection of structures with noisy data by an effective deep learning framework using autoencoder-convolutional gated recurrent unit. Ocean Eng. 243, 110142.
Wold, S., Esbensen, K., Geladi, P., 1987. Principal component analysis. Chemometr. Intell. Lab. Syst. 2, 37–52.
Wu, R.-T., Jahanshahi, M.R., 2019. Deep convolutional neural network for structural dynamic response estimation and system identification. J. Eng. Mech. 145, 04018125.
Yu, Y., Wang, C., Gu, X., Li, J., 2019. A novel deep learning-based method for damage identification of smart building structures. Struct. Health Monit. 18, 143–163.
Yu, Z., Shen, Y., Sun, Z., Ying, W., 2022a. Cracklab: A High-Precision and Efficient Concrete Crack Segmentation and Quantification Network. Developments in the Built Environment, 100088.
Yu, Y., Liang, S., Samali, B., Nguyen, T.N., Zhai, C., Li, J., Xie, X., 2022b. Torsional capacity evaluation of RC beams using an improved bird swarm algorithm optimised 2D convolutional neural network. Eng. Struct. 273, 115066.
Zhang, A., Wang, K.C., Fei, Y., Liu, Y., Chen, C., Yang, G., Li, J.Q., Yang, E., Qiu, S., 2019. Automated pixel-level pavement crack detection on 3D asphalt surfaces with a recurrent neural network. Comput. Aided Civ. Infrastruct. Eng. 34, 213–229.